Galectin-3 Binding to α 5 β 1 Integrin in Pore Suspended Biomembranes

Nirod Kumar Sarangi, Massiullah Shafaq-Zadah, Guilherme Berselli, Jack Robinson, Estelle Dransart, Aurélie Di Cicco, Daniel Lévy, Ludger Johannes, Tia Keyes

Galectin-3 binding to α5β1 integrin in pore suspended biomembranes

Nirod Kumar Sarangi[1∫], Massiullah Shafaq-Zadah[2∫], Guilherme B. Berselli[1ǂ], Jack Robinson[1ǂ], Estelle Dransart[2], Aurélie Di Cicco[3], Daniel Lévy[3], Ludger Johannes[2], and Tia E. Keyes[1]**

[1] School of Chemical Sciences and National Centre for Sensor Research, Dublin City University, Glasnevin, Dublin 9, Ireland.
[2] Institut Curie, Université PSL, U1143 INSERM, UMR3666 CNRS, Cellular and Chemical Biology unit, 75005 Paris, France.
[3] Institut Curie, PSL Research University, UMR 168, Centre de Recherche, 75248 Paris, France
∫ *Contributed Equally*
ǂ *Contributed Equally*
* Correspondence to tia.keyes@dcu.ie and ludger.johannes@curie.fr

Abstract

Galectin-3 (Gal3) is a β-galactoside binding lectin that mediates many physiological functions, including the binding of cells to the extracellular matrix for which the glycoprotein α5β1 integrin is of critical importance. To study their interaction, Gal3 and α5β1 integrin were purified, and the latter reconstituted into microcavity supported lipid bilayers composed of physiological eggPC:eggPA, which enabled multimodal interrogation of the membrane using electrochemical impedance and fluorescence lifetime correlation spectroscopies. Upon incubation with wild-type Gal3 (WTGal3) at low nanomolar concentrations, the membrane electrical resistance of α5β1 integrin-containing membranes decreased, while membrane capacitance, fluidity, and the lateral diffusivity of the integrin increased. These effects were much reduced or even absent when a Gal3 deletion mutant lacking the N-terminal oligomerization domain (Gal3ΔNter) was used, when lactose was present as a competitive inhibitor of glycan-WTGal3 interaction, or when WTGal3 or Gal3ΔNter were incubated with membranes in the absence of α5β1 integrin. These findings indicated that Gal3 oligomerized on α5β1 integrin in a glycan-dependent manner, and that the N-terminal domain interfered with membranes in a way that is yet to be fully understood. At concentrations above 10 nM of WTGal3, membrane capacitance started to decrease and very slowly diffusing molecular species appeared, which indicated the formation of a protein layer made from WTGal3-α5β1 integrin assemblies. In conclusion, our study demonstrates the capacity of WTGal3 to oligomerize in a cargo protein-dependent manner at low nanomolar concentrations. Of note, these WTGal3 oligomers appeared to have membrane active properties that had not been revealed before using our sensitive methods. At slightly higher WTGal3 concentrations, the capacity to generate lateral assemblies between cargo proteins was observed. In cells, this would lead to the construction of tubular endocytic pits according to the GlycoLipid-Lectin (GL-Lect) hypothesis, or to the formation of galectin lattices, depending on cargo glycoprotein specific or plasma membrane intrinsic parameters.

Significance statement

Upon expression from animal tissue, galectins are synthesized in the cytosol and translocated to the extracellular milieu by unconventional secretion. Galectins drive the endocytosis of glycoproteins such as $\alpha_5\beta_1$ integrin but also organize them into lattices. Although these notions are in apparent contradiction, we now envision a model in which galectin lattices and galectin-driven endocytosis cooperate to control the homeostasis of glycoproteins at the plasma membrane. The intricacies of the interactions between oligomerization competent galectins and glycoproteins that usually carry several glycans are still incompletely understood. In this work, we employed pore-suspended lipid bilayers as an *in vitro* platform to address the multivalent and specific carbohydrate-dependent interactions of galectin-3 with $\alpha_5\beta_1$ integrin.

1. Introduction

Integrins are transmembrane heterodimeric protein complexes comprised of alpha and beta subunits that integrate and mediate signals between the extra- and intracellular space via binding to different extracellular matrix ligands and numerous binding partners present at the cytosolic side of the plasma membrane (1). 24 integrins are known in vertebrates and all are

of significant biomedical importance. All integrins have common structural motifs including in the α domain a 7-bladed β propeller connected to a thigh and two calf domains. A metal ion-dependent adherent site (MIDAS) is also conserved and is crucial for ligand binding (2). Integrins regulate various biological functions such as cell adhesion, migration, proliferation, differentiation, and spreading, and the remodeling of the extracellular matrix (3). This ability to regulate crosstalk between the cell and the surrounding environment positions integrins as key players in the process of tumor progression, and different integrins are indeed expressed in different tumors (4). Overexpression of integrins leads to resistance in therapies, tumor reoccurrence and survival issues. $\alpha_5\beta_1$, integrin, also known as the fibronectin receptor, has been identified as a potential therapeutic target on certain solid tumors. For example, in breast cancer cell lines it has been observed that the ligation of β1 integrins, such as $\alpha_5\beta_1$ and $\alpha_2\beta_1$, with extracellular matrix components significantly reduces drug-induced apoptosis from chemotherapeutic agents (5).

Galectins are a family of 15 proteins that contain highly conserved carbohydrate-recognition domains (CRD) that allow binding to glycosylated proteins and lipids at the surface of cells or in the extracellular matrix, including integrins. Galectins access the extracellular milieu by unconventional secretion (6, 7). They have been classified into three subtypes, i) the prototype group, ii) the tandem repeat group and iii) the chimera group (3, 8–11). The prototype group has one carbohydrate-recognition domain, whereas the tandem repeat group consists of two carbohydrate-recognition domains separated by a linker sequence (12).

Galectin-3 (Gal3) is the sole representant of the third chimera galectin subtype. This lectin has an important role, in part mediated by integrins, in physiological and pathological phenomena (13) and is the most documented galectin family member. Gal3 is widely distributed in many tissues. It carries two specific domains, one CRD as for all galectin members, but also an intriguing N-terminal domain comprising of proline/glycine/tyrosine-rich repeats that is linked with its oligomerization capacity upon binding to surface glyco-receptors (14, 15), possibly involving liquid-liquid phase separation (16–18). Gal3 is reported to stimulate neutrophil adhesion and migration, spreading of cancer cell lines, and furthermore, promotes focal adhesion turnover and fibronectin fibrillogenesis in tumor cells (19–22). Gal3 has been linked to all sorts of diseases such as various types of cancers, type 1 diabetes, depression and Alzheimer's disease (5, 9, 23–25). Understanding and regulating the response of Gal3-integrin interactions is a critical biomedical challenge because lectin-integrin signaling is integral to many disease states (26, 27).

Galectins and notably Gal3 have been directly implicated in the regulation of the cell surface homeostasis of glycoproteins (28). They have been shown to favor the endocytic uptake of these glycoproteins (e.g., $\alpha_5\beta_1$ integrin (22, 29) via a mechanism that has been termed the glycolipid-lectin or GL-Lect hypothesis (30). According to this model, monomeric Gal3 in solution oligomerizes upon binding to cell surface glycoproteins such as integrins. Oligomeric Gal3 then acquires the capacity to interact with glycosylated lipids of the glycosphingolipid family in a way such as to drive the formation of tubular endocytic pits from which so-called clathrin-independent endocytic carriers form for the cellular uptake of the cargo glycoproteins. Initially described for Gal3 and the cellular uptake of CD44 and $\alpha_5\beta_1$ integrin (29), the GL-Lect hypothesis has more recently also been documented for galectin-8 and another specific cargo protein, CD166 (31). Although these findings are in apparent contradiction with earlier ones on galectins inducing lateral lattices that negatively affect endocytosis (32), we now envision a model in which galectin lattices and the GL-Lect mechanism cooperate to control the homeostasis of glycoproteins at the plasma membrane (33).

In vitro studies at artificial membrane platforms such as liposomes and supported lipid bilayers (SLBs) have been successfully applied to interrogate the interaction of membrane lipids as well as membrane embedded receptors with external biomolecules such as proteins and peptides (34–36). Although, they have provided much insight, there is room for improvement in biomimicry to closely match the experimental conditions *in vivo*. In the case of liposomes as membrane models, they are limited to the approaches that can be applied for analytical interrogation, e.g., they are not so amenable to study two-dimensional interfaces and there is limited flexibility in composition, i.e., as both leaflets are formed simultaneously asymmetric leaflet composition is challenging to achieve with precision (37, 38). While for SLBs, interference from the interfacial support (substrate effect) due to frictional/pinning on the fluidity and functionality of the bilayer and associated membrane proteins can limit biomimicry. Although, tethered membranes have been introduced using either an extra layer intervening between the substrate and lower leaflet, irrespective of whether this layer is tethered, e.g., through a covalently bound self-assembled monolayer or is a physio-absorbed polymer cushion, the biomimicry, whilst improved, remains unclear (35, 39–42). Nonetheless, the advantage of SLB-based approaches are, their greater compositional control and versatility in terms of experimental interrogation compared with liposomes (43–45). Particularly, when the solid support is conducting, this can be used as an electrode thus enabling electrochemical study of lipid-peptide/protein interaction (46–49).

Alternative approaches have emerged recently, that assembled membranes supported over buffer filled periodic pore structures which improve membrane fluidity, whilst maintaining stability. Most importantly, in the case of buffer filled pore

supported bilayers, they offer the advantage of a relatively deep aqueous reservoir, that SLBs lack, in contact with proximal leaflet (50–54). We recently exploited microcavity array suspended lipid bilayers (MSLB) formed at cavity array PDMS and gold electrodes to study receptor mediated interaction and detection of peripheral proteins such as cholera toxin B-subunit (55), hemaglutannin A1 (56), annexin V (57) and small molecule drug permeability (58–61), across varied lipid membrane compositions, and have demonstrated that they offer the fluidity of liposome/proteoliposomes with the addressability of SLBs. Here, we apply them to a biophysical study of $\alpha_5\beta_1$ integrin-Gal3 interaction.

2. Materials and Methods

Equipment and reagents

Rat livers (Charles Rivers), functionalized wheat germ agglutinin (WGA) agarose resin (Sigma-Aldrich, Ref. 61768-5 ml), NHS-activated agarose column functionalized with FN-$III_{9\text{-}10}$ (Ge Healthcare, NHS-HiTrap Ref. 17071701), pre-casted 4-15 % polyacrylamide gels (BioRad), 300-400 mesh carbon-coated copper grids for electron microscopy (Delta Microscopy, Ref. DG400-Cu), Hepes 1 M, pH 7-7.4 (Sigma-Aldrich, Ref. H0887), $MgCl_2$, $CaCl_2$, Triton X-100 (Anatrace, Ref. T1001-500 mL), *n*-dodecyl β-D-maltoside (DDM) (Cliniscience, Ref. D310-25GM), protease inhibitors (Sigma-Aldrich, Ref. P8849), PefaBlock® (Sigma-Aldrich, Ref. 76307), N-acetylglucosamine (GlcNac, Sigma-Aldrich, Ref. A8625-5G), sucrose, EDTA pH 8, egg phosphatidylcholine (ePC, Avanti polar, Ref. 840051C), porcine brain L-alpha-phosphatidylserine (bPS, Avanti Polar, Ref. 840101C), rhodamine B 1,2-dihexadécanoyl-*sn*-glycéro-3-phosphoéthanolamine (Thermofisher, Ref. L1392), HisPur™ Cobalt Resin (Termofisher, Ref. 89965), NHS-ATTO-488 (ATTO-TEC GmbH), NHS-Alexa647 (Invitrogen), non-reducing SDS-loading sample buffer, hamster anti-Rat β_1 integrin (BioLegend, Ref. 102202) primary antibody, HRP-coupled secondary anti-hamster antibody, ECL. Bio-Beads SM2 adsorbent media (Biorad, Ref. 152-3920), BioRad ChemiDoc for protein detection (chemiluminescence), automatic plunge freezer for cryo electron microscopy (CryoEM) sample preparation (EM-GP, Leica, Germany), 80 kV TECNAI G2 Lab6 electron microscope (Thermofisher, USA) for structural analysis.

Purification of $\alpha_5\beta_1$-integrin from rat livers

$\alpha_5\beta_1$ integrin was solubilized and purified as described in (62). Briefly, 4 rat livers (about 65 g in total) were cut in small pieces and incubated with lysis buffer (20 mM Hepes, 2 mM $MgCl_2$, 2 mM $CaCl_2$, 2 % (v/v) Triton X-100, protease inhibitor cocktail 1/250 dilution, Pefablock® 1/1000 dilution, pH 7.4), such that the liver tissue weight represents 25 % (w/v) of the total final volume of extraction. Tissues were two times homogenized using an ultra-Turrax® homogenizer, and incubated for 60 min at 4 °C on orbital shaker. The extract was centrifuged at 75,000 x g for 30 min at 4 °C. The supernatant was then centrifuged again using the same settings. The final lysate supernatant was clarified by filtration through a Whatman paper, and loaded on two 25 ml WGA-affinity columns connected in series, at a flow rate of 0.8 mL/min. Columns were washed with washing buffer (20 mM Hepes, 150 mM NaCl, 2 mM $MnCl_2$, 0.2 % (v/v) Triton X-100, protease inhibitor cocktail 1/250 dilution, Pefablock® 1/1000 dilution, pH 7.4), at a flow rate of 2 mL/min. Glycosylated proteins were finally eluted with washing buffer supplemented with 300 mM GlcNAc. Protein-enriched fractions were pooled and loaded on a 10 ml FN-$III_{9\text{-}10}$-functionalized column at a flow rate of 0.08 mL/min, to specifically bind $\alpha_5\beta_1$ integrin, using an FPLC purifier system. Unbound material was then removed with washing buffer at a flow rate of 0.2 mL/min. $\alpha_5\beta_1$ integrin was finally eluted with elution buffer (20 mM Hepes, 150 mM NaCl, 10 mM EDTA, 0.2 % (v/v) Triton X-100, Pefablock 1/1000, pH 7.4), at a flow rate of 0.08 mL/min.
For electron microscopy and negative staining characterization of purified $\alpha_5\beta_1$ integrin, protein extraction from rat livers was performed using DDM (Dodecyl maltoside) detergent instead of Triton X-100.
Protein purity and concentration were determined by SDS-PAGE analysis and Bradford colorimetric assay, respectively. Integrin-enriched factions were then pooled, snap-frozen and stored at -80 °C.

Negative staining and electron microscopy

4 µL of purified integrin diluted at a final concentration of 20 µg/mL (DDM-based extraction) were dropped on a pre-activated 300-mesh carbon-coated copper grid. Negative staining was performed with 2 % (w/v) uranyl acetate solution. Electron microscopy micrographs were acquired at 52 k magnification with 80 kV Tecnai electron microscope.

Reconstitution of $\alpha_5\beta_1$ integrin in small unilamellar vesicles (SUVs)

The reconstitution was performed at a lipid/protein ratio (LPR) of 10 (w/w). 200 µg of eggPC:eggPA (90:10, w/w) solubilized in chloroform were mixed and excess of organic solvent evaporated under nitrogen atmosphere. Lipidic films were dried under vacuum at room temperature for 2 h, and then resuspended in 150 µL of 20 mM Hepes, 150 mM NaCl pH 7.4. Lipids were then solubilized by adding 0.25 % (v/v) Triton X-100 and incubated for 10 min at 21 °C under gentle stirring. 20 µg of purified $\alpha_5\beta_1$ integrin was added to the solubilized lipids, the Triton X-100 concentration was adjusted to 0.5 % (v/v) in a 200

µL final reconstitution volume, and incubated for 10 min at 21 °C under gentle stirring. The detergent was eliminated by three consecutive additions of Bio-Beads SM2 (prepared according to manufacturer's instruction), 2 times with 10 mg, and one time with 20 mg, after 2 h, 1 h and 1 h time intervals, respectively. SUVs were transferred to a new tube and stored at 4 °C until use. The size of the integrin reconstituted SUVs was found to be ~120 nm estimated from Dynamic Light Scattering (DLS) using a Malvern, Zetasizer. Lipid and $\alpha_5\beta_1$ integrin final concentrations in SUVs were 1 mg/mL and 0.1 mg/mL, respectively.

Characterization of $\alpha_5\beta_1$ integrin incorporation into SUVs by sucrose gradient

For SUV visualization on sucrose gradient, 0.5 % (w/w) of rhodamine DHPE was added to the lipid composition of $\alpha_5\beta_1$ integrin/SUVs prepared as described above. In a cold room, 100 µL of $\alpha_5\beta_1$ integrin/SUVs were diluted to a final volume of 575 µL in 20 mM Hepes, 150 mM NaCl, 30 % (w/v) sucrose, pH 7.4, and placed at the bottom of a 2.5 ml polypropylene ultra-centrifuge tube. Sucrose gradient was then built by gently pouring, from the bottom to the top of the tube, 575 µL of 20 %, 10 %, 5 % and 0 % (w/w) sucrose solutions prepared in 20 mM Hepes, 150 mM NaCl pH 7.4 buffer. The sample was centrifuged at 100,000 x g (Beckman TLS55 rotor) for 16 h at 4 °C. Samples were collected from each sucrose gradient level, denatured in non-reducing SDS-sample loading buffer, boiled for 5 min and loaded on a 4-15 % pre-casted polyacrylamide gel. Proteins were then transferred on nitrocellulose membrane, and the presence of $\alpha_5\beta_1$ integrin in all fractions was immuno-detected by incubation with primary anti-rat β_1 integrin antibody, followed by secondary HRP-coupled anti-hamster antibody.

Characterization of $\alpha_5\beta_1$/SUVs morphology by cryo-electron microscopy

4 µL of $\alpha_5\beta_1$ proteoliposomes (1 mg/mL lipids, 0.1 mg/mL integrin) were loaded on a copper lacey carbon 300 mesh grid. After 30 sec incubation in a humid environment (85 % humidity), the sample was vitrified by blotting the excess sample on the opposite side from the liquid drop for 4 s and plunged frozen in liquid ethane. Images were acquired with a Tecnai G2 Lab6 electron microscope operated at 200 kV and equipped with a 4 K x 4 K CMOS camera (F416, TVIPS). Image acquisition was performed under low dose conditions of 12e-/Å2 at a magnification of 50,000 with a pixel size of 2.14 Å.

Characterization of $\alpha_5\beta_1$ orientation after reconstitution in SUVs

5 µL of $\alpha_5\beta_1$/SUVs were diluted with 5 µL of 20 mM Hepes, 150 mM NaCl pH 7.4 buffer, and incubated under agitation for 30 min at 20 °C with 10 µL of 200 µg/mL trypsin solution, either complemented with 0.5 % (v/v) Triton X-100 (total integrin digestion) or not (surface-exposed integrin digestion). Trypsin was inactivated with 10 µl of non-reducing SDS-sample loading buffer and boiled for 5 min at 95 °C. Samples were loaded on a 4-15 % pre-casted polyacrylamide gels and proteins were then transferred onto nitrocellulose membranes. Presence of $\alpha_5\beta_1$ integrin was immuno-detected by incubation with primary anti-rat β_1 integrin antibody, followed by secondary HRP-coupled anti-hamster antibody.

Functionality of $\alpha_5\beta_1$ integrin after reconstitution in SUVs

$\alpha_5\beta_1$ integrin integrity, once incorporated in SUVs, was assessed by its capacity to bind fibronectin. 20 µL of $\alpha_5\beta_1$/SUVs (2 µg of protein, 20 µg of lipids) were incubated for 30 min at 21 °C on a rotating wheel either with 2 mM $MgCl_2$ or $MnCl_2$ in 100 µl of 20 mM Hepes, 150 mM NaCl, pH 7.4 buffer. Histidine-tagged FN-$III_{9\text{-}10}$ fibronectin fragment was added at a 10 µM final concentration for 1h30 at 21 °C still under rotation. Reactions were loaded on 30 µl bed-volume of cobalt-coated beads and incubated for one additional hour at 4 °C on a rotating wheel. Unbound material was then removed and beads washed with 20 mM Hepes, 150 mM NaCl, pH 7.4 buffer, supplemented or not with 2 mM of $MgCl_2$ or $MnCl_2$. Proteins were eluted from the beads with 30 µl of non-reducing SDS-loading sample buffer and boiled 5 min at 95 °C. Samples were loaded on a 4-15 % pre-casted polyacrylamide gel and proteins were then transferred onto nitrocellulose membrane. Presence of $\alpha_5\beta_1$ integrin was immuno-detected by incubation with primary anti-rat β_1 integrin antibody, followed by secondary HRP-coupled anti-hamster antibody.

Labelling of $\alpha_5\beta_1$ integrin with ATTO-488 fluorophore

Triton X-100 purified $\alpha_5\beta_1$ integrin (20 mM Hepes, 150 mM NaCl, 0.2 % (v/v) Triton X-100) was incubated with a 10-molar excess of NHS-ATTO 488 for 2 h at 21 °C under gentle agitation.

The reaction was quenched by the addition of 20 mM Tris pH 7.4 for 20 min at 21 °C. Excess of NHS-ATTO 488 was then removed using 40 kDa cutoff desalting spin-columns equilibrated with 20 mM Hepes, 150 mM NaCl, 0.2 % (v/v) Triton X-100, according to manufacturer's instructions. Final protein concentration was assessed by BCA colorimetric assay.

Labelling of wild-type Gal3 (WTGal3) and Gal3ΔNter with Alexa647

WTGal3 or Gal3ΔNter at a final concentration of 2 mg/mL were incubated for 2 h at 21 °C under gentle shaking in PBS with 4 molar excess of NHS-Alexa647 dye, in the presence of 10 mM of β-lactose. Reaction was quenched with 20 mM Tris final concentration for 20 min at 21 °C. Unreacted dye was cleared using 7 kDa desalting columns equilibrated with PBS, according to manufacturer's instructions. Protein concentration and labelling efficiency were determined by measuring OD_{280} and OD_{647}, respectively.

Fabrication of microcavity array gold and PDMS substrate

Microcavity supported lipid bilayers were assembled across periodic pore arrays prepared in PDMS for fluorescence correlation studies, or in gold for electrochemical studies using polystyrene sphere templating methods previously described (56, 58, 60, 63). Briefly, gold microcavity arrays were prepared by gravity-assisted convective assembly of micro-sized polystyrene microsphere lithography and selectively modified with a self-assembled monolayer (SAM) of 1 mM 6-mercapto-1-hexanol as described elsewhere. The gold-microcavity arrays were prepared by drop casting polystyrene (PS) microspheres of 1 µm of diameter followed by gold electroplating, as described in the schematic presented in Figure 2C. To obtain a highly packed microcavity array, a highly closed packed monolayer of polystyrene (PS) microspheres were casted using gravity assisted method onto pre-cut rectangles of gold coated silicon wafers. Then, gold was electrodeposited onto the interstitial surface between the PS microspheres by applying a reduction potential (-0.6 V, Ag/AgCl) to the gold array in the presence of a cyanide free gold solution. The electrodeposition was controlled by the evolution of the current at the gold array until the current reached a minimum value corresponding to the closer distance between the spheres, indicating that the electrodeposition of gold has reached the hemisphere of PS. After the gold electrodeposition, the arrays were electrochemically cleaned using cyclic voltammetry in sulfuric acid (10 mM) for 6 cycles (-0.2 to 1.8 V) and rinsed with deionized water, ethanol and dried gently under nitrogen flow. The top surface of the gold microcavity arrays was then selectively functionalized with a self-assembled monolayer of 6-mercaptohexanol (1 mM) for at least 24 h in ethanol, before removal of the templating spheres which were subsequently washed out of the array with tetrahydrofuran (THF) (55, 61).
The PDMS microcavity arrays were prepared by drop casting 50 µL of ethanol containing 0.1 % of 4.61 µm polystyrene spheres (Bangs Laboratories) onto a 1 cm x 1 cm hand cleaved mica sheet. After ethanol evaporation, PDMS was poured onto the PS microspheres arrays and cured at 90 °C for 1 h. Microcavity arrays are then formed after removing the inserted PS microspheres by sonicating the PDMS substrate in THF for 15 min. The substrates were then left to dry overnight. Prior to lipid bilayer formation, the substrates were cleaned using oxygen plasma for 5 min and microcavities were buffer filled before lipid monolayer deposition by sonicating PDMS substrate in PBS or HEPES buffer (pH 7.4) for 1 h.

Fabrication of pore suspended lipid bilayers

Pore suspended lipid bilayers were prepared according to a two-step process described previously for a range of bilayer compositions (54, 57, 58, 60, 64). The proximal leaflet of eggPC monolayers was transferred by the Langmuir-Blodgett (LB) technique. Briefly, approximately 50 µL of eggPC (1 mg/mL in chloroform) were deposited onto the air-water interface of LB trough (NIMA 102D) and the solvent allowed to evaporate for 15 min. The resulting lipid monolayer at the air/water interface was compressed four times to a surface pressure of 33 mN/m at 25 mm/min. Then, the micro-cavity arrays were immersed into the LB trough until all of the cavities were submerged completely into the subphase. The micro-cavity array was then withdrawn from the trough at a rate of 5 mm/min whilst the surface pressure of the lipids was retained at 32 mN/m to ensure an adequate transfer of the eggPC monolayer. To assemble the upper leaflet of the bilayer, liposome fusion was carried out using SUVs prepared as described above, comprised of eggPC:eggPA (90:10). Where integrin was reconstituted into the MSLB, according to the procedure above, a proteoliposome was prepared at a lipid to protein ratio of 10 (L/P=10) and fused to the LB prepared monolayer (55, 57, 58). The integrity of the resulting PDMS or gold MSLBs was confirmed by FCS and by EIS, respectively.

Fluorescence lifetime correlation spectroscopy (FCS)

Fluorescence lifetime imaging and correlation spectroscopy measurements were performed using a Microtime 200 system (PicoQuant GmBH, Germany) integrated with FCS module, dual SPD detection unit, time-correlated single photon counting (TCSPC), on an inverted Olympus X1-71 microscope with an Olympus UPlanSApo 60x/1.2 water immersion objective. A single mode optical fiber guided the lasers to the main unit and provided a homogeneous Gaussian profile excitation beam. The lasers were pulsed at 20 MHz, corresponding to an interval of 50 ns. The emitted fluorescence was collected through the microscope objective. A dichroic mirror z532/635rpc blocked the backscattered light, and corresponding filters were used to clean up the signal. A 50 µm pinhole was set to confine the volume of excitation and detection of fluorescence intensity that originated from the fluorescently labelled protein in the axial direction. Fluorescence was detected using a single photon avalanche diode (SPAD) from MPD (PicoQuant). Before FCLS measurement, backscattered images of the substrate (images were taken using an OD3 density filter) followed by fluorescent life-time images were acquired to ensure the optimal

positioning of the buffer filled cavities where the bilayers are spanned. FLCS analyses the time-dependent fluctuations of the fluorescence intensity $\partial I(t)$ recorded over 30 s and analyzed by an autocorrelation function, $G(\tau) = \langle \partial I(t) \rangle \cdot \langle \partial I(t+\tau) \rangle / \langle \partial I(t) \rangle^2$, where $\langle\rangle$ denotes the time average, and $\langle\, \partial I(t) \rangle$ and $\langle\, \partial I(t+\tau) \rangle$ are the fluorescent intensity fluctuations around the mean value at time, t and $t+\tau$ respectively. The FLCS autocorrelation data fit to a 2D diffusion model equation defined in Eq. (1);

$$G(\tau) = \left(1 + \frac{f_T}{1-f_T} e^{-t/\tau_T}\right) \cdot \frac{1}{\langle N \rangle} \cdot \frac{1}{1+(\tau/\tau_D)^{\alpha}} \qquad (1)$$

where, $\langle N \rangle$ is the average number of diffusing fluorescence particles in the observation volume, f_T and τ_T are the fraction and the decay time of the triplet state, τ_D is the transit time, and α is the anomaly coefficient. From the fitting the τ_D values were evaluated and accordingly, the diffusion coefficient was obtained from Eq. (2);

$$D = \frac{\omega^2}{4\tau_D} \qquad (2)$$

where ω is the observation beam waist diameter typically obtained from calibration of a standard dye diffusing in 3D with known diffusion coefficient value. Point FLCS measurements were then recorded for a duration of 30 s per cavity, and an average of 20 cavities were studied for every FLCS measurement. All FLCS experiments were carried out in triplicate and at 20±1 °C.

Electrochemical impedance spectroscopy

Electrochemical impedance spectroscopy (EIS) measurement was performed with a CHI760e (CH Instrument, USA). A standard 3-electrode cell was employed for all measurements, comprised of gold microcavity array covered by lipid bilayer as a working electrode, an Ag/AgCl (1 M KCl) reference and a coiled platinum wire counter electrode. The EIS data were recorded across a frequency range of 0.05 to 10^5 Hz with an AC modulation amplitude of 10 mV at a DC potential bias of 0 V (vs Ag/AgCl). All measurements were carried out in a glass cell (approximate volume of 4 mL of either 0.01 M PBS or 0.01 M HEPES). The EIS of the aqueous filled microcavity array coated with the lipid bilayer composition alone was measured initially before the addition of protein to ensure signal stability. The non-Faradaic EIS signal from the integrin reconstituted MSLBs was evaluated for stability, and it was found that when placed in contact with the buffer, an initial fluctuation of resistance occured that stabilized within an hour and then remained unchanged over a prolonged 24 h window, which was well beyond our experimental time window (5-6 h) for WTGal3/Gal3ΔNter binding studies. Initially, for integrin reconstituted MSLBs, a time lag of 90-120 min was allowed to ensure that the membrane had equilibrated in the electrochemical cell (no fluctuation of EIS i.e., the membrane impedance is unchanged) before proteins were titrated. For each protein aliquot, the designated concentration of protein was added to the electrochemical cell and an equilibration binding time of 30 min was maintained. This window was confirmed to be sufficient for protein binding to the membrane, as beyond this time, protein binding elicited no further change to membrane impedance signal. The proteins (WTGal3 and Gal3ΔNter) were initially prepared as a stock solution in buffer and this was aliquoted into the electrochemical cell to achieve the required final concentration and mixed thoroughly. The volume added to the cell never exceed 200 µL. All measurements were carried out at room temperature (22±1 °C). The impedance of the MSLBs for each protein type as well as their temporal stability were assessed in triplicate. The measured data were analyzed using Z-View software (Scribner Associates, v3.4e) by fitting the equivalent circuit model (ECM) shown in Figure 2C. The best fit using the ECM circuit was assessed from both visual inspections of the fit residuals and χ2, typically ~ 0.001.

3. Result and Discussion

3.1 Purification, characterization and reconstitution of $\alpha_5\beta_1$ integrin within small unilamellar vesicles

$\alpha 5\beta 1$ integrin was solubilized in DDM detergent and specifically purified from rat liver as described in the methods section. We have used electron microscopy (EM) in negative staining mode to qualitatively validate the integrity of the DDM-micellar protein particles at the structural level. Purified micellar $\alpha_5\beta_1$ integrin clearly appeared as individual particles on the EM-grids that presented the typical shape of integrin heterodimer, including a globular head-piece and thinner leg parts (Figure 1A). Remarkably, many of these integrin particles were in the bent-closed inactive conformation, 10-15 nm in length and well-described for their low affinity for fibronectin (Figure 1A, inset, cartoon). This was fully consistent with our elution strategy, where the integrin was initially activated to efficiently bind the $FNIII_{9\text{-}10}$-functionnalized column. The subsequent release consisted of inactivating the integrin, which led to its elution from the column in the bent-closed conformation.

We then successfully incorporated the purified micellar-integrin (Triton X-100 micelles) into small unilamellar vesicles (SUVs) at a LPR of 10. Integrin density in SUVs was assessed by loading the reconstituted proteoliposomes onto sucrose gradients, followed by immunodetection of the protein in the fractions of each sucrose gradient. Interestingly, integrins were only detected at the middle and the top fractions of the 5 % sucrose gradient (Figure 1B). This suggests a homogenous distribution of the protein amongst the proteoliposome population and a low density of protein, as expected from the LPR used. Moreover, the absence of integrin in the fraction corresponding to the highest concentration of the sucrose gradient (here 30 %) indicates that no protein aggregation occurred during the reconstitution step.

Cryo-EM analysis was performed to assess both the morphology and size of the $\alpha_5\beta_1$ integrin proteoliposomes. As shown on the micrographs, these liposomes appeared as homogenous unilamellar and circular vesicles, with a mean diameter of 150 nm (Figure 1C, inset), suitable for subsequent reconstitution onto the microcavity suspended lipid bilayers (MSLB).
The proper orientation of $\alpha_5\beta_1$ integrin after reconstitution in SUV was then assessed. It is indeed critical to have a substantial fraction of integrin molecules that are correctly oriented within the proteoliposome with their cytosolic domain facing into the lumen. The trypsin-accessibility/protection assay was used to address this point. Proteoliposomes were incubated with trypsin in the absence of Triton X-100 for the immunodetection of the correctly orientated integrin fraction (Figure 1D, lane 1, scheme 1), or in the presence of Triton X-100 without trypsin (Figure 1D, lane 3, scheme 3) for evaluation of the total amount of incorporated integrin. The efficiency of enzymatic digestion was confirmed by the absence of β_1 integrin immunodetection (Figure 1D, lane 2, scheme 2) when SUVs were disrupted by Triton X-100 incubation before trypsin treatment, thus exposing the total pool of integrin to the enzyme.

Importantly, the proportion of correctly orientated integrin was estimated to be about 50 %, which is sufficient for our assays. We then aimed to confirm that our reconstituted $\alpha_5\beta_1$ integrin was functional. For this, we have assessed its capacity to become activated, either using $MgCl_2$ or $MnCl_2$ preincubation for integrin priming, followed by pull-down on fibronectin ($FNIII_{9\text{-}10}$) fragment-coated beads. Immunodetection of β_1 integrin in the presence of $MgCl_2$, and to a greater extent with $MnCl_2$, (Figure 1E) confirmed that even in a liposomal environment $\alpha_5\beta_1$ integrin retained its capacity to become activated and to interact efficiently with its natural ligand, fibronectin.

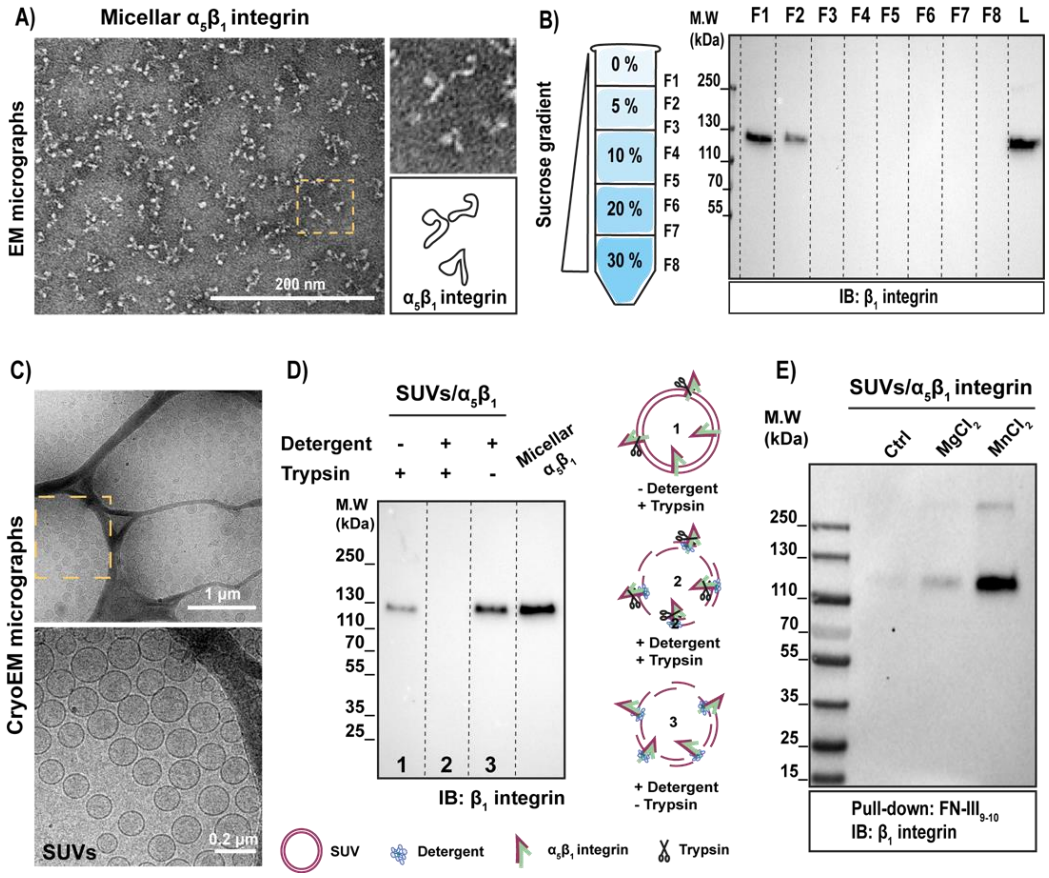

Figure 1: $\alpha_5\beta_1$ integrin purification and reconstitution into SUVs

(**A**) Qualitative visualization of $\alpha_5\beta_1$ integrin particles by EM. DDM-solubilized $\alpha_5\beta_1$ integrin from rat livers was purified on a fibronectin-functionalized column, EDTA-eluted and blotted onto carbon grids at a protein concentration of 20 µg/ml. Images were acquired by EM after negative staining of the samples. Inset shows a magnification of micellar integrin particles, and the cartoon box an illustration of individual integrins in the bent-closed conformational state. (**B**) Characterization on sucrose gradients of $\alpha_5\beta_1$ integrin incorporation into SUVs. Gradient fractions F1 to F8 (cartoon) were collected and submitted to anti-β_1 integrin immunoblotting. Corresponding to its molecular weight, β_1 integrin was detected at 120 kDa in F1 and F2. L represents total proteoliposomes input. (**C**) Homogeneity of the proteoliposomes as visualized by cryoEM. $\alpha_5\beta_1$ proteoliposomes were loaded on copper lacey carbon grids, and frozen. Inset shows a magnification view. The proteoliposomes were homogenous in size, with a mean diameter of 150 nm. (**D**) Analysis of $\alpha_5\beta_1$ integrin orientation within SUVs. Proteoliposomes were subjected or not to trypsin digestion in the presence or absence of Triton-X100. In the absence of detergent (lane 1), the immunoreactive band corresponds to β_1 integrin molecules for which the large extracellular domain was oriented into the liposomal lumen, and thereby protected from the protease. In the presence of trypsin and detergent (lane 2), no β_1 integrin band was detected, since the enzyme now had full access to the whole protein. In the presence of the detergent alone (lane 3) the detected band corresponds to the total amount of β_1 integrin. This allowed us to estimate the percentage of correctly oriented $\alpha_5\beta_1$ integrin, which was around 50 %. Micellar $\alpha_5\beta_1$ integrin was used as a control. The cartoon shows a schematic illustration of the different conditions. (**E**) Assessment of the functionality of liposomal $\alpha_5\beta_1$ integrin. To confirm the capacity of $\alpha_5\beta_1$ integrin to become activated, proteoliposomes were pre-incubated ($MgCl_2$ or $MnCl_2$) or not (Ctrl) with the indicated activating metal ions, and then submitted to fibronectin FN-$III_{9\text{-}10}$ pull down. As expected, β_1 integrin was pulled down in the presence of magnesium ($MgCl_2$) and to a greater extent in the presence of manganese ($MnCl_2$), demonstrating that the SUV-reconstituted integrins were functional.

3.2 Characterization of proteoliposomes using DLS and FCS

The liposomes for the outer leaflet of MSLB were obtained by standard methods, or as described in the experimental section in the case of $\alpha_5\beta_1$ integrin-reconstituted liposomes. Dynamic Light Scattering (DLS), was used to follow the steps of proteoliposome preparation. The initial eggPC:eggPA liposomes resuspended in Hepes buffer formed vesicles of narrow size distribution with a mean diameter of 500 nm shown in Figure S1a, Supplementary Information (SI). Detergent disruption was confirmed from the change in the size distribution of liposomes (Figure S1b, SI). Following detergent removal, the reformed proteoliposomes containing $\alpha_5\beta_1$ integrin showed fairly homogeneous radii of 120 nm (Figure S1c, SI). Additionally, using fluorescence life-time cross-correlation spectroscopy (FLCCS), the diffusion of labelled $\alpha_5\beta_1$ integrin-ATTO488 and DOPE-ATTO655 in proteoliposomal bilayer was evaluated following simultaneous excitation of both fluorophores (Figure S1d, SI). The autocorrelation function (ACF) showed that $\alpha_5\beta_1$ integrin and DOPE co-diffused, confirming that both were indeed reconstituted into the same proteoliposomes.

3.3 Electrochemical characterization of Gal3 binding to PC:PA membranes with or without integrin

3.3.1 Electrochemical characterisation of MSLB without and with the presence of $\alpha_5\beta_1$ integrin

The fabrication of hexagonally packed microcavity pore (1 µm diameter) arrays in gold (1×1 cm^2) and the assembly of bilayer without or with integrin for use in non-Faradaic electrochemical impedance spectroscopy (EIS) studies were performed according to our previous reports (56, 58, 61, 64). In the absence of integrin, the bilayer comprised of eggPC in the proximal leaflet and eggPC:eggPA (90:10) in the distal leaflet, hereafter called PC//PC:PA membrane. The PC monolayer was transferred via Langmuir-Blodgett method followed by fusion of PC:PA LUVs. The formation of integrin reconstituted bilayer, hereafter called PC//PC:PA/Int, was achieved via transfer of an eggPC monolayer by the Langmuir-Blodgett followed by fusion of proteoliposomes consisting of $\alpha_5\beta_1$ integrin reconstituted into PC:PA(90:10) SUVs (~120 nm) at a LPR of 10.
The characterization of these microcavity array suspended bilayers was carried out using EIS. Figure 2A shows representative non-Faradaic Nyquist plots obtained from EIS measurements at pristine gold cavity arrays (black), eggPC:eggPA (90:10) bilayer assembled at the array (blue) and integrin reconstituted PC//PC:PA MSLB (red). The corresponding frequency-normalized complex capacitance plots are shown in Figure 2B. The non-Faradaic Nyquist trace shows the sum of real (Z′) and imaginary (-Z′′) components of the complex impedance, which reflect any changes to the ion transfer process across electrode/electrolyte interface. For example, when the Nyquist trace shifts towards the x-axis (Z′), the impedance is decreased, or admittance (ion transport) is increased. Similarly, a shift towards the y-axis (-Z′′) implies that the impedance is increased, and admittance decreased. It is clear that upon PC//PC:PA (blue) bilayer formation, the impedance was increased compared to the SAM-functionalised cavity array support (black) and increased further when $\alpha_5\beta_1$ integrin was present in the PC//PC:PA membrane (red) (Figure 2A, inset). In addition, the electrode capacitive properties on assembly of lipid/integrin can be visualized from the angular frequency-normalized complex capacitance plot (Y''/ω vs Y'/ω), as shown in Figure 2B. The semicircle plot intercepts in Y''/ω at ~$40\times10^{-6}\ F$ for a SAM-modified cavity (black) was significantly reduced

to 3.2×10^{-6} F when the PC//PC:PA membrane was assembled (blue), and the intercept further decreased to 2.1×10^{-6} F when integrin α5β1 integrin was reconstituted at the PC//PC:PA membrane (Figure 2B, inset). Quantitative evaluation of changes to membrane electrical resistance and capacitance properties was extracted by fitting the EIS data to the equivalent circuit model (ECM) (Figure 2C). We previously reported this heuristic approach which was used here for the MSLB model (60, 61).

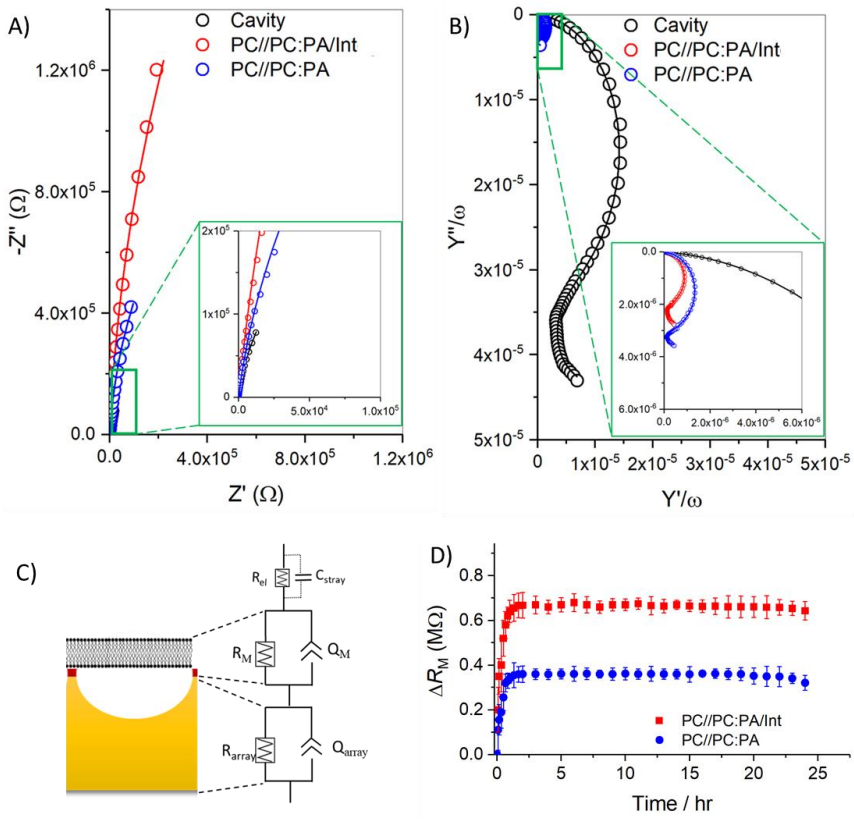

Figure 2. EIS characterization of pristine and integrin containing MSLB. Non-Faradaic (**A**) Nyquist plot and (**B**) frequency normalized complex capacitance plot of the cavity array (black), PC//PC:PA spanned over cavity array (blue) and integrin spanned PC//PC:PA/Int MSLB (red). In both panels (A,B) zoomed-in areas are shown in insets highlighted in green box. (**C**) Schematics of MSLB spanned over a cavity array (not to scale) and the associated equivalent circuit model (ECM) used to fit EIS data. In the ECM, R_{el}, and C_{array} represent respectively solution electrolyte resistance and stray capacitance, R_M and Q_M represent respectively membrane resistance and constant phase element (CPE), and R_{array} and Q_{array} are the microcavity array resistance and CPE. The corresponding fits to the ECM are shown as solid lines in panels A and B. (**D**) Relative change in membrane resistance to show the stability of PC//PC:PA membranes without (blue) and with (red) the presence of $\alpha_5\beta_1$ integrin versus time monitored for more than 24 h. The EIS recording at an initial time window of 0-1.5 h shows an increase in membrane resistance which saturates and remains stable for more than 24 h. EIS measurements were performed in 0.01 M PBS buffer within the frequency ranges between 0.05 Hz to 10^5 Hz at 0 V DC bias potential vs Ag/AgCl (1 M KCl) with an AC amplitude of 10 mV at 22±1 °C. A three-electrode set-up where gold cavity/MSLB, Ag/AgCl (1 M KCl) and Pt coiled served as working, reference, and counter electrodes, respectively.

In fitting the EIS data (Figure 2A, B, solid lines), representative absolute resistance values for SAM-modified cavity arrays without bilayer, with PC//PC:PA bilayer and PC//PC:PA integrin-reconstituted membranes were determined as 0.4±0.15, 7.7±0.5 and 9±0.8 MΩ, respectively. Similarly, the capacitance (Q) values of the constant phase element (CPE) were estimated as 40±3, 3.4±0.2 and 2.5±0.3 μF·S^{m-1}. Q is analogous to the magnitude of the capacitance, and m is the constant phase, which is a frequency independent real number that varies between 0<m<1 (typically for MSLB, m=0.94±0.02) (61). , The greater resistivity and reduced capacitance of the protein containing membrane confirms integrin reconstitution. The non-Faradaic EIS signal after the formation of MSLB comprised of PC//PC:PA with and without $\alpha_5\beta_1$ integrin was monitored to evaluate membrane stability. When MSLB was initially placed in contact with PBS buffer, we observed an initial increase in resistance ($\Delta R_M = R_M^{time=t} - R_M^{time=0}$) over 0-1.5 h for both pristine and to a greater extent for $\alpha_5\beta_1$ integrin-containing PC//PC:PA membranes, that then remained stable over a prolonged time window of 24 h (Figure 2D). This 24 h window of stability is well beyond our experimental time window (5-6 h) for the lectin binding studies (vide infra).

3.3.2 Electrochemical characterisation of Gal3 binding to MSLB in the absence of $\alpha_5\beta_1$ integrin

EIS was used as a highly sensitive, label-free measurement modality to study how Gal3 influences membrane phase or packing. First, we compared the impact of WTGal3 on the membrane resistance of the PC//PC:PA MSLBs to determine if interactions between the lectin and membrane occur in the absence of integrin. After an equilibration time of 2 h, the WTGal3 concentration was increased in a step-wise manner in the contacting solution at the PC//PC:PA membrane. After each WTGal3 addition, an incubation time of ~30 min was applied before EIS was recorded. The changes to membrane resistance and capacitance values were extracted by fitting the EIS data to the equivalent circuit model (ECM) described above. These values were reported as ΔR and ΔQ rather than absolute values to avoid the influence of batch to batch variation in substrate dimensions. However, in each instance the absolute resistance of the protein-reconstituted membrane was evaluated, to ensure it was conform to the expected R and Q values of stable lipid bilayers, as described above and previously.(58, 61) The relative changes in membrane resistance (ΔR) and capacitance (ΔQ) were defined as ($R_M^0 - R_M^{lectin}$) and ($Q_M^0 - Q_M^{lectin}$), where R_M^0 and Q_M^0 represent respectively the absolute resistance and capacitance of pristine membranes, i.e., in the absence of lectin, and R_M^{lectin} and Q_M^{lectin} the respective values when lectin was present in the contacting solution.

As shown in Figure 3A (black), incubation of WTGal3 with the PC//PC:PA membrane elicited a modest but systematic decrease in membrane resistance with increasing protein concentration. The response saturated at a WTGal3 concentration of ~37 nM. The decreased membrane resistance was consistent with the increased diffusivity of the membrane reported in FCS studies vide infra and may be due to phase changes or nanopore formation in the membrane induced by WTGal3. In contrast, a Gal3 mutant in which the unstructured N-terminal oligomerization domain was deleted (termed Gal3ΔNter) did not elicit any measurable change in membrane resistance (Figure 3A, red). Correspondingly, the capacitance of the membrane was not influenced significantly up to 60 nM of Gal3ΔNter (Figure 3B, red), whereas WTGal3 caused a small initial increase to capacitance that stabilised at 10 nM (Figure 3B, black). An increase in capacitance typically suggests membrane thinning. Although the capacitance change was very small at only ~0.1 $\mu F \cdot S^{m-1}$. Together with the significant decrease in membrane resistance, the data indicate WTGal3 interacts with the membrane and increases its permittivity. This may be explained by an electrostatic interaction of negatively charged PA head groups with positive charge density on the carbohydrate recognition domain of Gal3 that is positively charged at physiological pH of 7.4(15), or by penetration of the partially lipophilic proline-rich N-terminal domain(16) into the lipid membrane possibly inducing some surfactant-like nanoporation(65). The absence of impact of the N-terminal deleted lectin on membrane electrical properties is suggestive of the latter.

3.3.3 Electrochemical characterisation of Gal3 binding to $\alpha_5\beta_1$ integrin-containing MSLB

EIS experiments were then performed on PC//PC:PA membranes containing $\alpha_5\beta_1$ integrin (L/P=10, w/w). Substantially greater changes to membrane resistance and capacitance were observed upon incubation of Gal3 with integrin reconstituted MSLB (PC//PC:PA/int) compared to membrane without integrin (Figure 3C, D). In addition, the slopes of the curves of the EIS response in presence of integrin were steeper. Notably, both WTGal3 and Gal3ΔNter caused a decrease in resistance of the integrin-containing bilayer (Figure 3C). The magnitude of resistance changes was found to be consistently roughly twice as great for WTGal3 compared to Gal3ΔNter. Strikingly, opposing results were observed for WTGal3 and Gal3ΔNter when capacitance data were recorded. While for WTGal3, the membrane capacitance increased at concentrations up to 10 nM, it then decreased at higher concentrations (Figure 3D, black), whereas we observe a continuous decrease in capacitance for Gal3ΔNter that saturated at 10 nM (Figure 3D, red).

For WTGal3, the initial increase in capacitance indicated, along with the decreased resistance, that membrane permittivity increased, suggesting that WTGal3 reorganized the membrane and influenced its packing. Although an initial capacitance increase was also observed in the absence of $\alpha_5\beta_1$ integrin (Figure 3B, black), its amplitude was much greater at integrin-containing membranes (Figure 3D, black), which indicated that the glycoprotein strongly favoured the recruitment of the lectin. Since this increase in capacitance was not observed with Gal3ΔNter (see above), we conclude that it was due to the N-terminal domain of WTGal3. We speculate that the formation of Gal3 oligomers on $\alpha_5\beta_1$ integrin organizes and/or orients the hydrophobic proline-rich N-terminal domain of the lectin in a way such that it perturbs membrane organization, possibly by creating membrane domains and/or pores (see Conclusions). WTGal3 has indeed been shown to interact directly with lipids(65).

At WTGal3 concentrations above 10 nM, membrane resistance stabilised but capacitance decreased suggesting progressive thickening of the membrane (Figure 3D, black). This might originate from the formation of WTGal3-$\alpha_5\beta_1$ integrin assemblies that would grow laterally as membrane invagination cannot occur in the MSLB system. This view is supported by imaging

and FCS data, vide infra. Of note, the WTGal3 effect on permittivity persisted under these conditions as resistance remained at a low plateau level (Figure 3C, black) and capacitance — even if decreasing with the continued addition of WTGal3 above 10 nM — globally also remained above the level that was observed in the absence of the lectin (Figure 3D, black). We speculate that the permittivity and thickening effects occur concomitantly at WTGal3 concentrations above 10 nM.

The disaccharide β-lactose binds into the core pocket of the glycan recognition site on galectins (13). It can therefore be used as a competitive inhibitor of interactions that depend on this binding pocket. We found that the effects of WTGal3 and of Gal3ΔNter on the capacitance of $\alpha_5\beta_1$ integrin-containing membranes were effectively cancelled out in the presence of β-lactose (Figure 3E,F). It could thereby be concluded that these effects were indeed dependent on glycan-lectin interactions. In agreement with this conclusion, the corresponding resistance data (Figure S3, SI) also followed the same trend. In contrast, lactose had no effect on membrane impedance in the absence of Gal3 (Figure 3E,F), which confirmed the specificity of our findings.

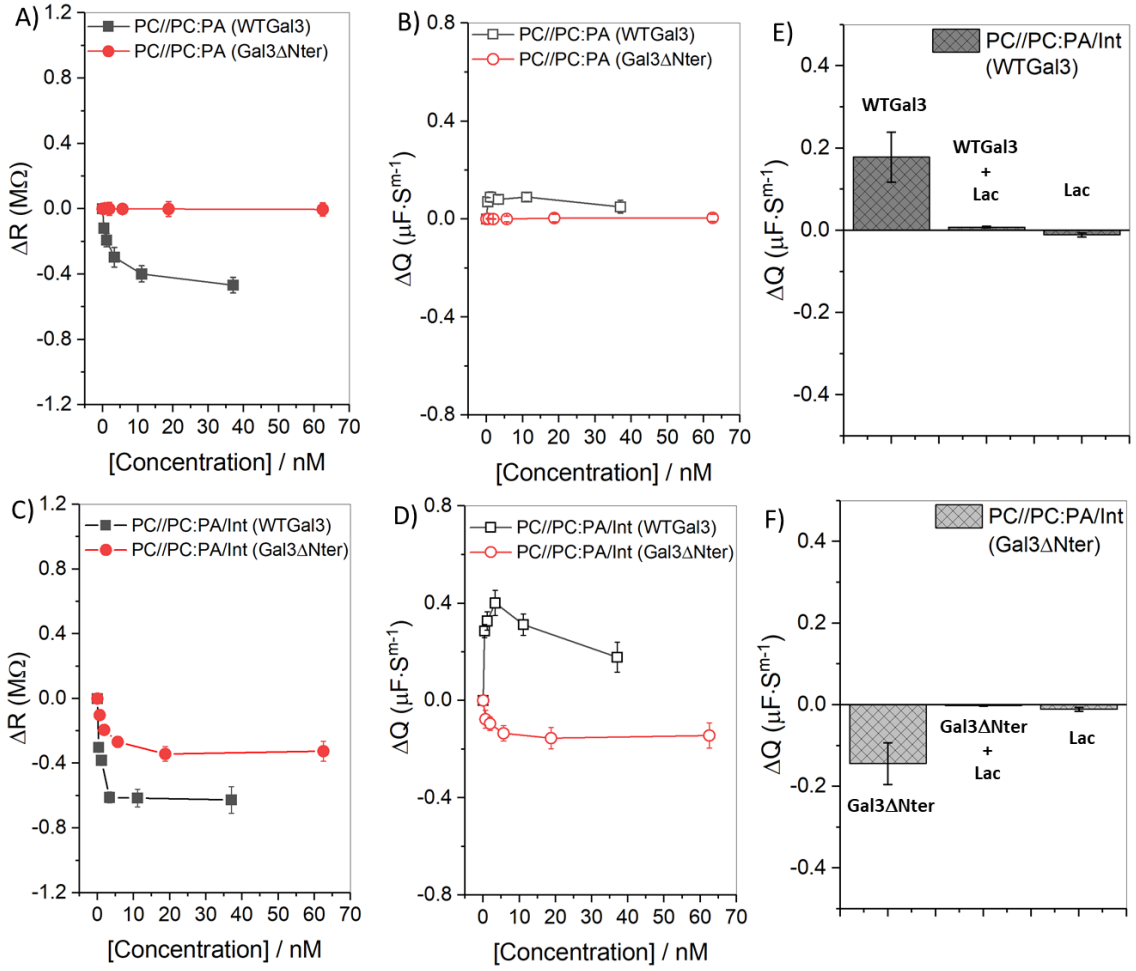

Figure 3. ***EIS characterization of pristine or integrin-containing membranes upon binding of WTGal3 or Gal3ΔNter***. (**A,B**) Relative change in (A) resistance, ΔR (filled symbol), and (B) capacitance, ΔQ (open symbols) values obtained upon binding of different concentrations of WTGal3 (black) or Gal3ΔNter (red) to PC//PC:PA membranes. (**C**,**D**) Relative changes in resistance (ΔR) and capacitance (ΔQ) values respectively obtained upon binding of different concentrations of WTGal3 (black) and Gal3ΔNter (red) to PC//PC:PA membranes into which $\alpha_5\beta_1$ integrin was reconstituted. The solid lines in each panel A-D are shown to guide the eye. Data are means ±SD from triplicate experiments. (**E,F**) Bar charts showing the change in capacitance values with respect to the pristine PC//PC:PA/Int membrane capacitance values when WTGal3 (E) or Gal3ΔNter (F) were incubated with $\alpha_5\beta_1$ integrin-containing membranes in the presence (+Lac) or absence of β-lactose. Lactose fully abolished the WTGal3 or Gal3ΔNter effects on ΔQ. In the absence of Gal3, lactose did not affect ΔQ. The concentration of WTGal3, Gal3ΔNter and β-lactose were 37 nM, 62.5 nM and 50 mM, respectively. EIS measurements were performed in 0.01 M PBS buffer, frequency ranges were from 0.05 Hz to 10^5 Hz at 0 V DC bias potential vs Ag/AgCl (1 M KCl) with an AC amplitude of 10 mV at 22±1 °C. Cell was a three-electrode set-up where gold cavity/MSLB, Ag/AgCl (1 M KCl) and Pt coiled served as working, reference, and counter electrode respectively.

To obtain quantitative empirical insight into the association of WTGal3 and Gal3ΔNter with pristine or $\alpha_5\beta_1$ integrin-containing membranes, the experimental ΔQ data (Figure 3B,D) were fit (Figure S2, SI) to the empirical Hill-Waud binding model according to Eq. 3;

$$\Delta Q = \frac{\Delta Q_{sat}(C)^n}{(K_D)^n + (C)^n} \qquad (3)$$

where ΔQ is the change in membrane capacitance, ΔQ_{sat} is absorption capacity or change in capacitance at maximum surface loading that relates to the number of available binding sites, k_D is the empirical apparent equilibrium dissociation constant, C is the concentration of the lectin (WTGal3 or Gal3ΔNter) and n (dimensionless) is the Hill coefficient, which reflects the steepness of the slope of the binding curve, often related to cooperativity, where it exists, in protein-receptor binding. n<1 is taken to indicate negative cooperativity, i.e., in chemically mediated adsorption where binding reduces affinity for further binding events, n = 1 reverts the expression to the Langmuir isotherm, where all binding sites are energetically equal, i.e., non-cooperative equilibrium binding, and n > 1 indicates positive cooperativity, where binding promotes affinity for further binding. From the fitting, a k_D of 0.2±0.02 nM was obtained when WTGal3 bound to the integrin containing PC//PC:PA membrane, versus a k_D of 0.76±0.04 nM for Gal3ΔNter binding. The fitting parameter values are reported in Table 1.

Table 1. Evaluation of dissociation binding constant, k_D, cooperativity, n, and maximum saturable absorption capacity, ΔQ_{sat} of WTGal3 and Gal3ΔNter upon binding to PC//PC:PA or PC//PC:PA/Int membranes.

lectinT	Membrane type	k_D (nM)	ΔQ_{sat} (μF·S^{m-1})	n	R^2
WTGal3	PC//PC:PA/Int	0.2±0.02	0.35±0.05	1.7	0.95
WTGal3	PC//PC:PA	0.09 ±0.02	0.08±0.01	1	0.99
Gal3ΔNter	PC//PC:PA/Int	0.76± 0.04	-0.15±0.01	0.8	0.96
Gal3ΔNter	PC//PC:PA	-	-	-	-

While the comparison between WTGal3 and Gal3ΔNter for the binding to $\alpha_5\beta_1$ integrin is relevant, k_D values for binding to membranes with or without $\alpha_5\beta_1$ integrin cannot be directly compared as they reflect on different types of interactions. In the first case, the primary binding site of the Gal3 proteins was $\alpha_5\beta_1$ integrin, and their effects on membranes needed to mediated from there. In contrast, in the absence of $\alpha_5\beta_1$ integrin, the primary binding site was the membrane itself, and the magnitude of EIS signal change was therefore expected to be greater.

From Table 1, the apparent k_D for the WTGal3 is approximately 3 times greater than that of Gal3ΔNter (Table 1). While this finding is qualitatively in agreement with the differential effect of both proteins on the capacitance change (ΔQ_{sat}) (Figure 3B), the amplitude difference between WTGal3 and Gal3ΔNter was much higher for ΔQ_{sat} than for k_D. This indicates much larger changes to membrane packing upon binding of WTGal3. This is notably emphasized by the steep slope of the plot (Figure 3D, open black symbol) and the Hill coefficient (n) in the presence of integrin (Table 1). The n of 1.7 for WTGal3 suggests a positive cooperative binding, likely due to Gal3 oligomerization upon binding on integrin. In contrast, n decreased to 0.8 in the case of the Gal3ΔNter, as expected for this oligomerization deficient mutant.

3.4 FCS-based characterization of Gal3 binding to pristine or $\alpha_5\beta_1$ integrin-reconstituted membranes

Our EIS data indicate that WTGal3 recognizes $\alpha_5\beta_1$ integrin reconstituted into PC//PC:PA membranes via a carbohydrate-dependent interaction. Furthermore, the distinct behaviour of WTGal3 and Gal3ΔNter suggests that integrin promotes not only WTGal3 binding, but also its oligomerization, which in turn is key to promoting high affinity association. To further support these EIS data, we performed fluorescence lifetime-based imaging and fluorescence correlation spectroscopy. We have hence measured the diffusivity of membrane lipid probes, $\alpha_5\beta_1$ integrin and Gal3 using fluorescently labelled species. The measurements were carried out in analogous MSLBs formed at a periodic pore array, which for optical studies were fabricated in PDMS. Membranes were prepared both with and without ATTO488-labelled $\alpha_5\beta_1$ integrin, and Alexa647 was used to label WTGal3 and Gal3ΔNter.

3.4.1 FCS characterization of MSLB containing α5β1 integrin

As for EIS experiments, the microcavity array suspended eggPC lipid monolayer was first prepared by Langmuir-Blodgett transfer followed by vesicle fusion with PC:PA liposomes, without or with reconstituted $\alpha_5\beta_1$ integrin. The substrate for photophysical measurement was prepared from PDMS rather than gold as this provides a low reflectance medium. The pore

array for optical studies was incorporated into a microfluidic chamber that permitted introduction of reagents to the MSLB with minimum volume (55–57). The fluidity of the PC//PC:PA MSLBs was evaluated prior to reconstitution of integrin using a fluorescently labelled lipid, ATTO655-DOPE (0.01 mol %), which was doped only at the outer leaflet of the MSLB during liposome preparation. The diffusion coefficient of the membrane was estimated by fitting the ACF to the 2D diffusion model Eq. (1), and the diffusion coefficient was obtained from Eq. (2) as 6.66 ± 0.38 μm²/s with an anomalous factor (α) of 0.94 ± 0.17, indicating Brownian diffusion. The diffusion coefficient for the PC//PC:PA MSLBs was considerably lower than recorded for simple DOPC MSLBs, which were previously reported as approximately 10.5 μm²/s (55, 58). However, the value matches very well to diffusion value reported for DNA tethered lipid bilayer membrane patches of eggPC(66). This reflects the greater viscosity of the natural eggPC:eggPA lipids that were used here (67). In control experiments, the PC//PC:PA MSLB was confirmed stable by FCS over windows of at least 48 hours, well exceeding the experimental window for subsequent lectin binding studies (data not shown).

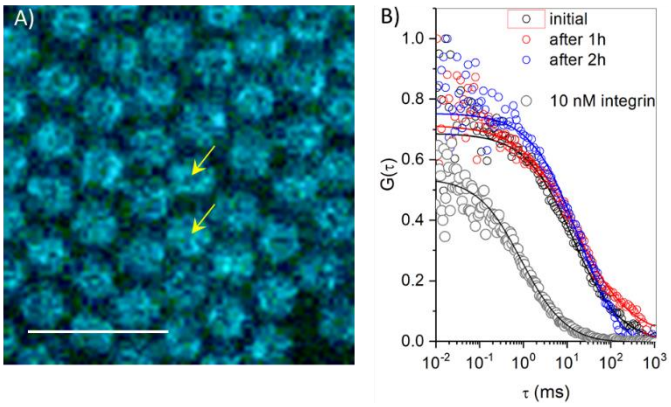

Figure 4. FLIM and FLCS characterization of integrin spanned across MSLB. (**A**) FLIM image of ATTO488-labelled $\alpha_5\beta_1$ integrin reconstituted into a PC//PC:PA MSLB. Brighter circles indicate zones in which the membrane was suspended over pores. Arrows in (A) indicate typical regions at the center of the pores where FCS was acquired from. The scale bar is 10 μm. (**B**) ACFs for ATTO488-$\alpha_5\beta_1$ integrin at different time points (black, red and blue) post-reconstitution into MSLBs, along with 10 nM ATTO488-$\alpha_5\beta_1$ integrin in micellar form diluted in PBS (grey). Solid lines are the fitted data for integrin diffusion across MSLB and solution using the 2D diffusion model, Eq. (1), and the pure diffusion model, Eq. S1(SI), respectively. The FCS data were collected and averaged from approximately 80-100 points from pores across the substrate. ACF traces show no changes over 6 hour windows. Both FLCS and FLIM images were taken over PDMS cavity array, the substrate is sealed within a microfluidic chamber filled with PBS (pH = 7.4) at 22±1°C.

Table 2. Estimated diffusion coefficients and corresponding anomalous (α) parameter of ATTO488-$\alpha_5\beta_1$ integrin in solution and in MSLBs along with lipid diffusion in PC//PC:PA MSLBs in the presence or absence of integrin. PC//PC:PA_Int indicates membranes reconstituted with integrin and PC//PC:PA without. Data from FLCS studies in PBS at pH 7.4. The SD are from triplicate measurements.

Diffusing fluorophores	***D* (μm²/s)**	***α***
ATTO488-$\alpha_5\beta_1$ in solution	46 ± 5	1.01±0.03
ATTO488-$\alpha_5\beta_1$ in PC//PC:PA_Int MSLBs	1.99 ± 0.56	0.86 ± 0.05
ATTO655-DOPE in PC//PC:PA MSLBs	6.66 ± 0.38	0.94 ± 0.17
ATTO655-DOPE in PC//PC:PA_Int MSLBs	5.40 ± 0.40	0.98 ± 0.10

Successful reconstitution of ATTO488-labelled $\alpha_5\beta_1$ integrin into MSLBs was confirmed by monitoring both FLCS and FLIM at the PDMS platform. Compared to the pristine bilayer, the decreased diffusion coefficient of the lipid marker ATTO655-PE from 6.66 ± 0.38 μm²/s to 5.40 ± 0.40 μm²/s indicated that $\alpha_5\beta_1$ integrin influenced membrane viscosity. Yet, lipid diffusion remained Brownian with an α of 0.98 (Table 2). Representative FCS autocorrelation data along with FLIM images are shown in Figure 4. The diffusion coefficient of the labelled ATTO488-$\alpha_5\beta_1$ integrin at the MSLB was measured as 1.99 ± 0.56 μm²/s with an α value of 0.86 ± 0.05 in contact with PBS. This value is ~22× slower when compared to solution diffusivity (46 ± 5

$\mu m^2/s$) of ATTO488-$\alpha_5\beta_1$ integrin in its micellar form (PBS, 0.2 % Triton X-100) at a concentration of 10 nM (Table 2). The diffusion of integrin, its molecular brightness and α value were observed to remain unchanged over a measurement period of 6-8 h which well exceeded the time window for the lectin binding studies. Interestingly also, the ATTO488-$\alpha_5\beta_1$ integrin diffusion was impacted by the identity of contacting buffer whereby, when HEPES was used, the average diffusion coefficient was measured at 2.76 $\pm$ 0.36 $\mu m^2/s$, instead of 1.99 ± 0.56 $\mu m^2/s$ in PBS. However, α was unchanged. Such buffer effects have been noted previously for other membranes (57, 68).

The diffusion coefficient obtained for $\alpha_5\beta_1$ integrin indicated its proper reconstitution into the MSLB, and the values were comparable to previously reported data for reconstituted integrins in GUVs (69). Our values also compared quite well with reconstituted platelet integrin $\alpha_{IIb}\beta_3$ reconstituted into DOPC or into a complex membrane composition at MSLBs, where diffusion coefficients of 3.20 ± 0.59 $\mu m^2/s$ and 2.80 ± 0.56 $\mu m^2 s^{-1}$ were reported, respectively, with α coefficients of approximately 1 in these matrices (54, 69). The lower diffusion values obtained here is attributed to the greater viscosity of the eggPC:eggPA mixture and in particular to the greater protein loading in the current protocol where in the originating liposomes a 1:10 protein to lipid ratio is expected to be faithfully translated to the MSLB. Moreover, the α was less than one, indicating sub-diffusion of $\alpha_5\beta_1$ integrin under our conditions, which we attribute to the crowded protein environment compared to our earlier reports where integrin was less than 1:100 protein to lipid ratio. (54, 69)

3.4.2 WTGal3 and Gal3ΔNter diffusivity measurements across MSLB in the absence of integrin

In order to first investigate any underlying interactions between WTGal3 or Gal3ΔNter and the pristine PC//PC:PA membrane, FLIM and FLCS measurements were carried out at MSLBs at PDMS arrays. Figure 5 shows a representative reflectance image obtained from the PDMS cavity array depicting the buffer filled cavities (white circles). The successful assembly of bilayer over the cavity array was ascertained from the FLIM image of 0.01 mol% ATTO532-DOPE (Figure 5B) in the upper leaflet of PC//PC:PA membranes. As expected, in the absence of labelled WTGal3, no emission was observed from the membrane (Figure 5C) using the 647 nm emission channel. Consistent with EIS data, WTGal3 was observed to adsorb at integrin-free PC//PC:PA membranes, where, even at the lowest concentration, imaging showed fluorescence from the labelled Galectin across the array (Figure 5D, left). The emission intensity remained largely unchanged on further addition of WTGal3 beyond 18.5 nM, also consistent with the EIS data, indicating that adsorption was saturated at this concentration. To further confirm whether the observed emission was confined to the membrane, the diffusion coefficient of the labelled WTGal3 was measured at the membrane. The data showed the emergence of two populations of WTGal3 with distinct diffusivities, depending on the concentrations of WTGal3: a mobile, lower prevalence population that was observed at lower concentration of Gal3 (Figure 5F, filled symbol), and a dominant population observed at high concentrations that showed very low mobility (Figure 5F, open symbol). The respective diffusivity values were found to be 6.5$\pm$0.15, which matches closely to the diffusivity of the lipid probe and 0.1$\pm$0.08 $\mu m^2/s$, obtained by fitting the ACFs to the 2D diffusion model of Eq. (1) The latter may be due to self-aggregation or preferential association of this population with any gel-phases within the membrane. Over the described range of concentrations, unlabelled WTGal3 also modestly influenced the diffusivity of the lipid label ATTO655-DOPE, which increased from 6.6 to ~6.9 $\mu m^2/s$ (Table 3). We concluded that membrane packing appeared to be somewhat disrupted by WTGal3, which was consistent with the decrease in resistance observed by EIS (Figure 3C).

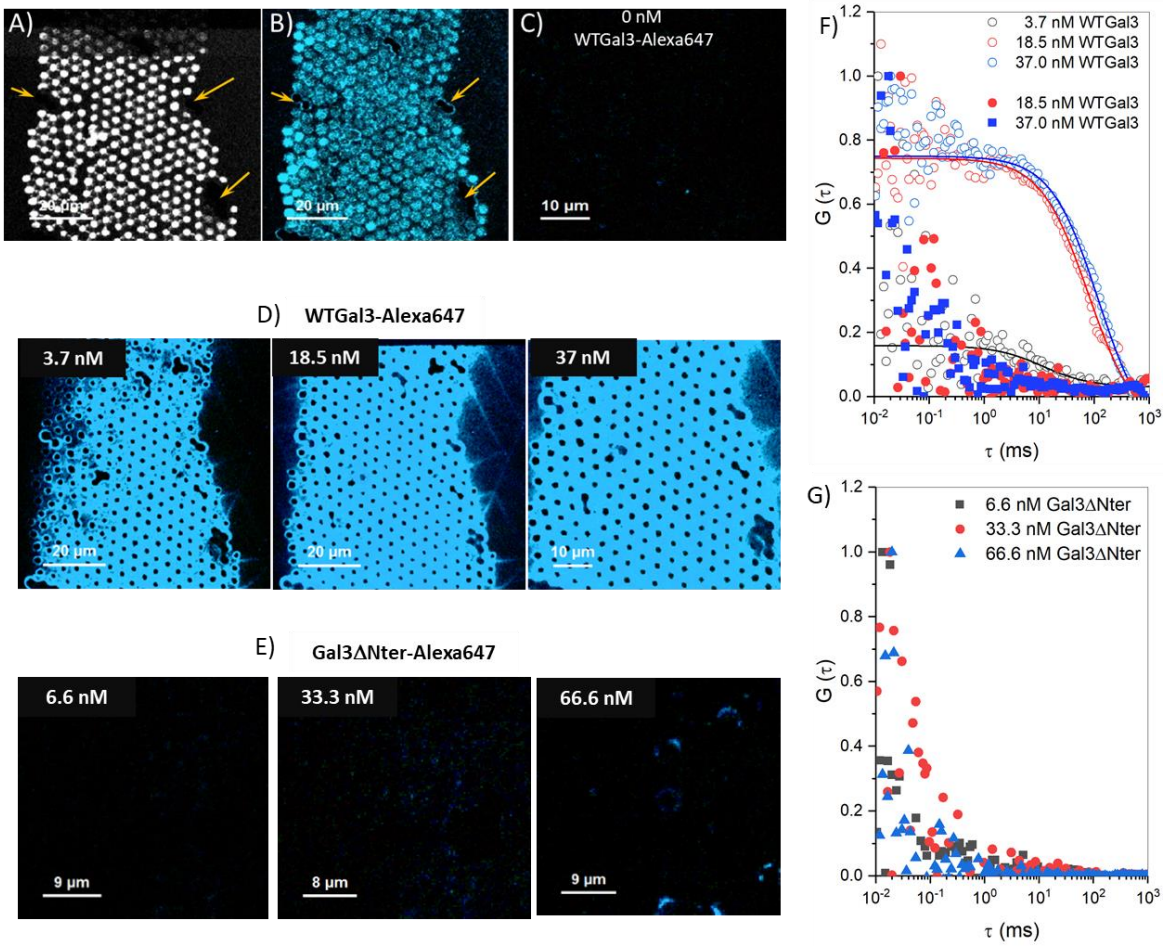

Figure 5. FLIM and FLCS characterization of pristine membranes upon binding of WTGal3 or Gal3ΔNter. (**A**) Reflectance and (**B**) FLIM image of pristine PC//PC:PA membrane labelled with ATTO532-DOPE (0.01 mol %). (**C**) FLIM image from the emission channel corresponding to the galectin label i.e., at 647 nm, when no WTGal3-Alexa647 (0 nM) was added to PC//PC:PA membrane. Arrows in panel (A) and (B) show cavities that were not filled with buffer and where no bilayers were formed. (**D**) and (**E**) represent FLIM images of Alexa647-labelled WTGal3 and Gal3ΔNter, respectively, at varying concentrations upon binding to PC//PC:PA membranes. (**F**) ACFs showing the diffusion of WTGal3-Alexa647 upon binding to PC//PC:PA membranes at different concentrations. Two regions could be distinguished in the array; open symbols (black, red and blue) show the experimental ACF for 3.7, 18.5 and 37 nM of WTGal3-Alexa647, where extensive aggregation causes slow diffusion, and filled circles (red:18.5 nM and blue: 37 nM) are not diffusing due to weak binding to membrane. Solid lines are the 2D fit using Eq (1). (**G**) ACFs of Gal3ΔNter-Alexa647 at varying concentrations (square: 6.6 nM, circle: 33.3 nM and triangle: 66.6 nM) upon binding to PC//PC:PA membrane. For each concentration of WTGal3-Alexa647 and Gal3ΔNter-Alexa647, FLIM imaging and FLCS were acquired after lectin incubation for 30 min and washes of the PC//PC:PA membrane with fresh PBS at 22±1 °C.

Table 3. Estimated diffusion coefficient values of lipids and proteins along with the anomalous factor, α. The SD are from triplicate measurements.

Diffusing fluorophores	D **(µm²/s)**	α
ATTO532-DOPE in PC//PC:PA	6.6 ± 0.38	0.94±0.17
ATTO532-DOPE in PC//PC:PA after 37 nM WTGal3	6.99 ± 0.12	0.86 ± 0.05
ATTO532-DOPE in PC//PC:PA after 66.6 nM Gal3ΔNter	6.7 ± 0.11	0.97± 0.15
WTGal3-Alexa647 in solution	83 ± 3	1±0.1
WTGal3-Alexa647 in PC//PC:PA (mobile fraction)	6.5 ± 0.15	0.94 ± 0.17
WTGal3-Alexa647 in PC//PC:PA (immobile/aggregates)	0.1± 0.08	0.86± 0.11
Gal3ΔNter-Alexa647 in PC//PC:PA	27 ± 5	0.98 ± 0.10

Under identical conditions, much lower association of Gal3ΔNter was observed at the PC//PC:PA membrane (Figure 5E,G). Despite the very weak signal, a diffusion coefficient of 27 ± 5 $\mu m^2/s$ was calculated, which is too high for a membrane insertion process, but too low for free diffusion. This diffusion coefficient value was likely to be attributed to a weak physisorption of the protein at the bilayer interface possibly due to electrostatic interactions between the Gal3's C-terminus domain and PA in the membrane.

Interestingly, when 37 nM of WTGal3-Alexa647 was incubated with PC//PC:PA membranes in the presence of 50 mM β-lactose, we observed very little signal from FLIM imaging, a low ACF signal in FLCS, and a much more modest increase in lipid diffusivity (Figure S4, SI). Consistent to the previous statement, β-lactose seemed to inhibit WTGal3 "non-specific" membrane interaction by preventing its lactose-occupied CRD domain to interact with the membrane.

Overall, we speculate that native WTGal3 behaves like an amphiphile: its hydrophobic N-terminus and its positively charged C-terminus may both interact with the membrane bilayer, causing the observed decrease in membrane resistance in EIS and altered membrane viscosity (16). Our observations are strongly consistent with findings of Lukyanov et al who reported, on the basis of fluorescence studies, that galectin-3 binds to phospholipids and can penetrate liposomal and cell membranes(65). As described, the effect is inhibited by lactose and suggests that the sugar induces structural changes in the galectin beyond the CRD. Indeed it has been reported that self-association between Gal3 molecules (which are not glycosylated) is impeded by lactose(70, 71).

3.4.3 WTGal3 and ATTO488-$\alpha_5\beta_1$ integrin diffusivity measurements across MSLB

The WTGal3-Alexa467 diffusivity in solution was measured at various concentrations from 3.7 to 37 nM and was found to be 83 ± 3 $\mu m^2/s$ in PBS (Figure 6C, grey circle). From the intensity-time trace throughout 20 independent recordings over 10 sec we did not observe any aggregate intensity spikes or any bleaching, suggesting that even at the highest concentration of WTGal3, the lectin remained monomeric in solution (Figure S5, SI). Using FCS, we then studied the association of Alexa647-labelled WTGal3 or of Gal3ΔNter with PC//PC:PA membranes into which $\alpha_5\beta_1$ integrin was reconstituted. Based on the intensity of the signal, the extent of membrane association of WTGal3 appears to be greater at the $\alpha_5\beta_1$ integrin-containing membrane compared to the pristine membrane, and absolute emission intensity increased in a concentration dependent manner, as shown in the FLIM images of the Alexa647 channel (in Figure 6A, left, top to bottom). The diffusivity of WTGal3 reduced drastically to below 4 $\mu m^2/s$ (Table 4). On analysis, this comprised of two diffusing components: A slow diffusing component, especially at higher concentrations (1.07 and 0.43 $\mu m^2/s$ for 18.5 nM and 37 nM, respectively; Figure 6C and Table 4) likely indicating clustering, and a mobile fraction with a diffusion coefficient that reached a plateau at highest protein concentration (3.54 ± 0.28 and 3.59 ± 0.11 $\mu m^2/s$ for 18.5 nM and 37 nM, respectively; Figure 6D and Table 4). The alteration of diffusivity could not merely be attributed to membrane association as the diffusive behaviour of WTGal3 was clearly very different when integrin was present in the membrane.

While two mobile WTGal3-Alexa647 populations emerged at the membranes in presence and absence of $\alpha_5\beta_1$ integrin, important differences existed. In the absence of integrin, the diffusivity of the mobile population at 6.5 ± 0.15 $\mu m^2/s$ (Table 3) matched closely that of the ATTO655-DOPE lipid at 6.66 ± 0.38 $\mu m^2/s$ (Table 2). In contrast, in the presence of $\alpha_5\beta_1$ integrin, the mobile WTGal3-Alexa647 component exhibited a much lower diffusivity of 2.51 and 3.54 ± 0.20 $\mu m^2/s$ at 3.7 or 18.5 nM of the lectin, respectively (Table 4), which follows the same trend as the diffusion coefficients of the integrin. Similarly, for the immobile population of WTGal3-Alexa647, diffusivity increased from 0.1 ± 0.08 $\mu m^2/s$ at the pristine membrane to 0.43 ± 0.15 $\mu m^2/s$ when the integrin was present. The fact that Gal3 diffusivity varied in the presence of $\alpha_5\beta_1$ integrin suggested their co-association in both, the slow and fast moving components,where from FCS we observe photobleaching of the integrin when galectin is present, attributed to immobilised integrin (Figure S6 A). And cross-correlation between integrin and WTGal3-Alexa647 was evident in FCCS studies discussed below for the fast component (Figure S6 B)

WTGal3 was observed to increase the diffusivity of $\alpha_5\beta_1$ integrin in MSLB membranes by at least 2-fold compared to the original diffusion value (Figures 6D and 7, Table 4). This was accompanied by an increase in alpha to nearly 1 (Table 4), indicating a switch from sub-diffusion to normal diffusion regime. As described above, the interaction of the WTGal3 with the underlying membrane was observed to decrease its viscosity and this is expected to contribute, at least in part, to this effect. However, both the greater magnitude of the change and alteration in diffusion regime indicate that other parameters are at play here. These may include changes to membrane phase or modulation of nanopore formation by WTGal3 when the integrin is present. However it is important to note that it is also likely that only a subpopulation of integrin remains mobile after galectin treatment and observed by FCS. Indeed, integrin tied up in immobile lattices would not contribute to the FCS signal, except as a background bleach which is evident in the time trace and immobilisation of the integrin at the lattice will deplete the concentration of mobile integrin in the bilayer. It has been shown previously that increased concentration of

membrane proteins increases membrane viscosity slowing the diffusion of lipids and of the proteins themselves(72–74) and this may well explain why we observe increased diffusion of integrin and reduction of alpha as the remaining mobile integrin in the bilayer is in a less crowded environment when the galectin sequesters the integrin into immobile networks.

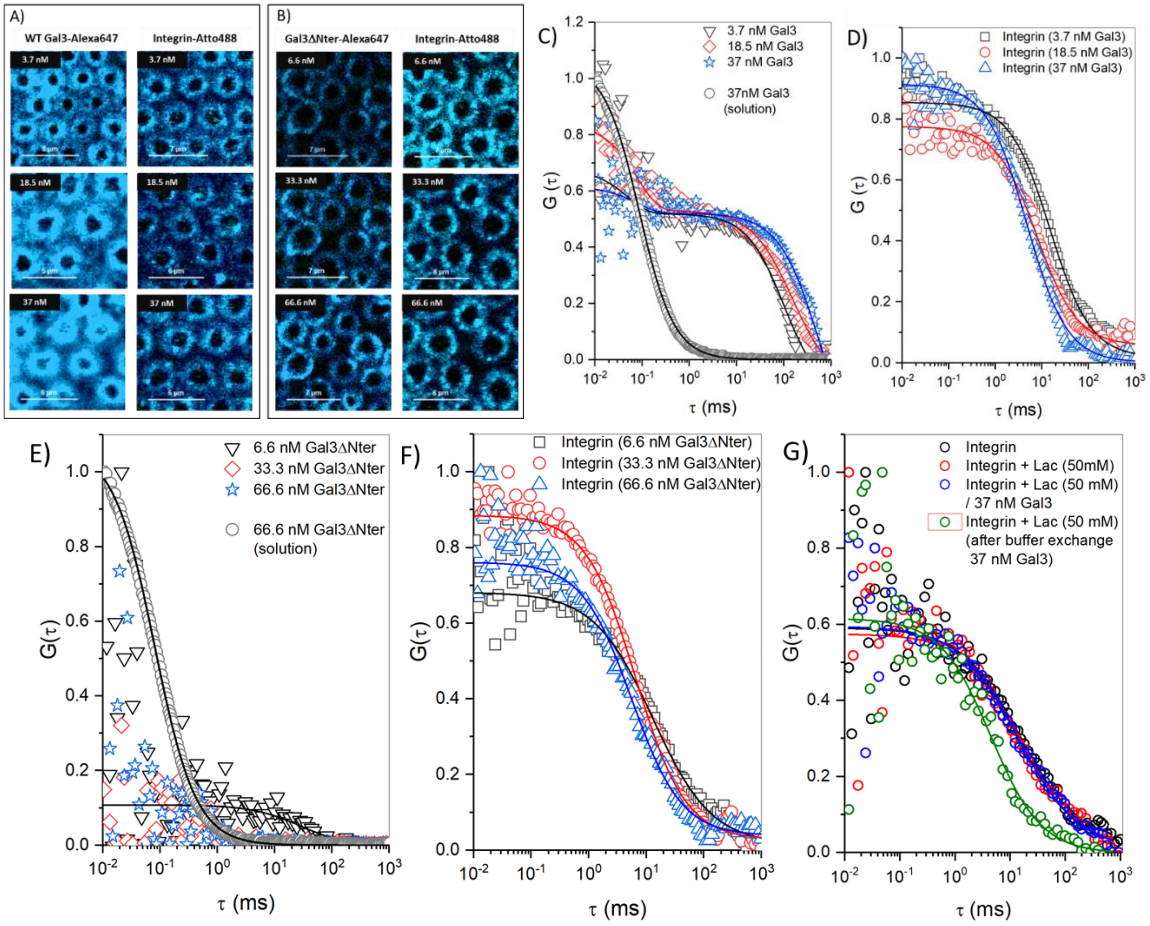

Figure 6. FLIM and FLCS characterization of WTGal3 and Gal3ΔNter upon binding to $\alpha_5\beta_1$ integrin-containing membranes. FLIM images of (**A**) WTGal3-Alexa647 (*left*) and (**B**) Gal3ΔNter-Alexa647 (*left*) at varying concentrations upon binding with PC//PC:PA/Int membrane. The corresponding ATTO488-$\alpha_5\beta_1$ integrin FLIM images are shown to the *right* in both panels. (**C**,**E**) ACFs of WTGal3-Alexa647 (C) and Gal3ΔNter-Alexa647 (E) at varying concentrations when bound to $\alpha_5\beta_1$ integrin-containing PC//PC:PA membranes. (**D**,**F**) ACFs of ATTO488-$\alpha_5\beta_1$ integrin upon binding of different concentrations of WTGal3-Alexa647 (D) or Gal3ΔNter-Alexa647 (F). (**G**) ACFs of $\alpha_5\beta_1$ integrin-ATTO488 reconstituted into PC//PC:PA membranes (black circle) in the presence of 50 mM β-lactose (red circle), of 37 nM WTGal3 in the presence of 50 mM β-lactose (blue circle), or after exchanging the contact solution of WTGal3+Lac with fresh 37 nM WTGal3 (olive circle). In all panels (C-G) open symbols represent the experimental data. Solid lines are the corresponding fit using eq. (2) except that a pure diffusion model equation (Eq.S1, SI) was utilized to extract the diffusion coefficient values from Alexa-labelled WTGal3 and Gal3ΔNter solution diffusivity measurements. All measurements were carried out in 0.01M PBS buffer of pH 7.4 and at 22±1 °C.

Table 4. Averaged diffusivity values of $\alpha_5\beta_1$ integrin-Atto488 without and with varying concentrations of WTGal3-Alexa647, and the WTGal3-Alexa647, diffusion values from the same experiments and fit to two components. The associated anomalous factor are provided. $\alpha_5\beta_1$ integrin was reconstituted into PC:PA (90:10) membranes at a LPR of 10. Values were collected in a single measurement from 80-100 cavity pores with each experiment repeated in triplicates at fresh membrane substrates. The SD were extracted from triplicate measurements.

Protein diffusion type at MSLB	***D* (μm²/s)**	***α***
Integrin before WTGal3	1.99 ± 0.56	0.85 ± 0.26
Integrin after 3.7 nM WTGal3	4.31 ± 0.24	1.02 ± 0.26
Integrin after 18.5 nM WTGal3	5.01 ± 0.09	0.93 ± 0.20
Integrin after 37 nM WTGal3	5.26 ± 0.23	0.92 ± 0.02
3.7 nM WTGal3	2.51 ± 0.28	0.96 ± 0.12

18.5 nM WTGal3	3.54 ± 0.11	0.96 ± 0.08
	1.07 ± 0.15	0.84± 0.10
37 nM WTGal3	3.59 ± 0.16	0.92 ± 0.12
	0.43 ± 0.15	0.75 ± 0.18

Figure 7 traces the trends in integrin and galectin diffusivities upon incubation with increasing concentrations of WTGal3. Integrin and the fast moving component of WTGal3 followed the same trend towards increased diffusivity when the concentration of WTGal3 was increased. However, the diffusivity values were not identical between integrin and WTGal3. Different explanations may be proposed for this. WTGal3 sub-populations will exist that are not involved in binding to integrin but merely associated with the membrane, thus contributing to lower the mean diffusion values of the fast component of WTGal3 diffusivity. For $\alpha_5\beta_1$ integrin, it needs to be considered that the protein was randomly oriented in the reconstituted membranes (Figure 1), with 50 % of the molecules not exposed to WTGal3. Notwithstanding any immobile integrin, the observed diffusivity values for $\alpha_5\beta_1$ integrin is therefore likely to be the mean of 2 subpopulations of which only one was in contact with WTGal3. At WTGal3 concentrations of 18.5 nM and above, when the slow diffusivity component of the lectin appeared, $\alpha_5\beta_1$ integrin diffusivity apparently reached a plateau. This behaviour could be due to the WTGal3-driven emergence of large $\alpha_5\beta_1$ integrin clusters. These interpretations are in line with a recent study where upon addition of WTGal3 to HeLa cells, lateral mobility of β_1 integrin as well as the size of clusters involving the integrin were increased (75).

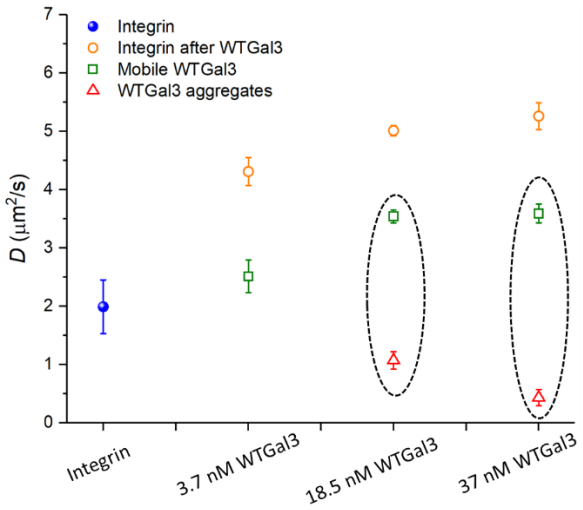

Figure 7. Diffusivity of $\alpha_5\beta_1$ integrin and WTGal3. Diffusivity of ATTO488-$\alpha_5\beta_1$ integrin and of WTGal3-Alexa647 at the indicated concentrations of the latter. The blue filled circle shows the diffusion coefficient value for ATTO488-$\alpha_5\beta_1$ integrin at MSLB before WTGal3 addition. Orange circles are the diffusion coefficient values of ATTO488-$\alpha_5\beta_1$ integrin following incremental addition of WTGal3-Alexa647 (3.7 nM, 18.5 nM and 37 nM). Green squares show the fast component of concentration dependent diffusion coefficient values for WTGal3-Alexa647 after binding to ATTO488-$\alpha_5\beta_1$ integrin containing PC//PC:PA membranes, and red triangles the ones of the slow diffusing component. Diffusion value in the presence of WTGal3-Alexa647 were obtained following 30 min incubation at the membranes at the indicated concentrations. Dotted oval marks highlight the bimodal diffusivity values of WTGal3-Alexa647.

3.4.4 Oligomerization capacity of Gal3 is essential for efficient $\alpha_5\beta_1$ integrin/Gal3 complex formation

Compared to WTGal3, Gal3ΔNter-Alexa647 associated much more weakly with ATTO488-$\alpha_5\beta_1$ integrin containing membranes, as revealed by much weaker signal intensity from the FLIM imaging (Figure 6B, left panel). The solution diffusivity of Gal3ΔNter-Alexa647 in the absence of membranes was found to be 90 ± 5 μm²/s (Figure 6E, grey circle) and the Gal3ΔNter ACF signal was too weak to reliably measure diffusivity from the membranes (Figure 6E, black, red and blue symbols). Furthermore, in contrast to WTGal3, the diffusion coefficient of ATTO488-$\alpha_5\beta_1$ integrin was unaffected by incubation with Gal3ΔNter-Alexa647 and remained constant at approximately 1.9±0.2 μm²/s over all lectin concentrations that were explored (Figure 6F). That we saw evidence for weak physisorption of Gal3ΔNter in EIS measurement but not by FCS, can be attributed to the fact that in the EIS experiments, the galectin was retained in the contacting solution during measurements whereas in the microfluidics device used for FCS, blank buffer was exchanged to reduce any background contribution from unbound fluorophore. Furthermore, association of WTGal3 with remaining mobile integrin was observed (Figure S6A, SI) as reflected in modest but significant cross-correlation data (Figure S6B, SI) obtained from spatial FLCS measurements. The cross correlation signal is weak, presumably because much of the integrin-galectin is tied up in immobile network and the FCCS signal reflects residual integrin-WTGal3 complex that diffuse, from the FCCS signal, with the same D

as the integrin. (it is important to remember that 50% of the integrin is in the "upside down" orientation and this is unlikely to bind to galectin or become immobilised at the galectin network so the weak FCCS signal can be attributed to remaining correctly oriented integrin, that remains mobile in the membrane and forms a complex with non-networked galectin). No such cross-correlation was obtained with Gal3ΔNter-Alexa647 on $\alpha_5\beta_1$ integrin-ATTO488 containing membranes. Of note, no WTGal3-induced clustering of integrin was observed from intensity time traces obtained from multi-channel-scalers (MCS) when integrin was in micellar form (Figure S6C, SI). Nonetheless, unlike MSLBs, the diffusivity of integrin was modestly increased in its micellar form upon WTGal3 addition as illustrated from ACFs traces (Figure S6D, SI). Overall, both measurements are consistent with a weak binding of Gal3ΔNter to integrin, which in the absence of the N-terminus oligomerization domain does not translate into the type of robust interaction and clustering capacity that is seen with WTGal3.

In the presence of 50 mM β-lactose (Lac), the increase of ATTO488-$\alpha_5\beta_1$ integrin diffusivity upon WTGal3-Alexa647 binding was no longer observed (Figure 6G). As a control we showed that the diffusivity of ATTO488-$\alpha_5\beta_1$ integrin itself was not influenced by 50 mM β-lactose incubation and remains stable at 1.9 ± 0.7 (Figure 6G). Furthermore, exchange with blank buffer with freshly added WTGal3 Alexa647 (37 nM), caused the diffusivity of $\alpha_5\beta_1$ integrin-ATTO488 to increase to 5.5 ± 0.8 $\mu m^2/s$ (α=0.98) (olive, Figure 6G).

In conclusion, as with EIS experiments, the FCS data establish that $\alpha_5\beta_1$ integrin is recognised by WTGal3 at the membrane in a glycan-dependent manner. This efficient $\alpha_5\beta_1$ integrin/Gal3 complex formation and the consecutive measurable membrane electrophysical modulations fully rely on a functional Gal3, where both C-terminus carbohydrate recognition and N-terminus oligomerization domains appeared to be essential features.

Conclusions

We have successfully reconstituted the purified transmembrane glycoprotein $\alpha_5\beta_1$ integrin into a microcavity suspended lipid bilayer (MSLB) platform of complex lipid composition, and applied electrochemical tools and fluorescence microscopy to study $\alpha_5\beta_1$ integrin/Gal3 complex formation and lateral membrane diffusivity. Use of cavity supported lipid bilayers with their deep aqueous reservoirs at both membrane interfaces permits native-like lateral fluidity of reconstituted membrane protein and enables versatile multimodal interrogation. This original and sensitive approach allowed us to provide a novel investigative angle to understand the specific functions of the C-terminal glycan binding and the N-terminal oligomerization domains of Gal3, in the presence of a naturally glycosylated cargo protein, $\alpha_5\beta_1$ integrin.

EIS experiments demonstrated that even in the absence of $\alpha_5\beta_1$ integrin, WTGal3 associates with membranes comprised of PC//PC:PA, evident through membrane resistance decrease (ΔR) that showed a systematic and saturable response with increasing WTGal3 concentration and followed Langmuir behaviour. FCS data showed, consistent with EIS data, that the WTGal3 influences membrane viscosity, modestly increasing the diffusion coefficient of the lipid marker and reducing its alpha to below 1.

Importantly, our EIS data show that WTGal3 associates with glycosylated $\alpha_5\beta_1$ integrin, in contrast to membrane alone, in a positive cooperative manner (n=1.7) with capacitance decreases not evident in the pristine membrane that indicated significant thickening of the membrane at WTGal3 concentrations above 10 nM. This is attributed, to Gal3 driven lateral condensation of $\alpha_5\beta_1$ integrins into lattices, resulting in the observed global thickening of the bilayer evident as decreased membrane capacitance. This proposal is supported by FLIM imaging, where integrin clusters seem to reorganize between 3.7 nM and 18.5 nM of WTGal3, to then increase in size between 18.5 and 37 nM. These changes were not observed with polymerization deficient mutant, Gal3ΔNter and were inhibited in the presence of lactose indicating the changes were carbohydrate dependent.

FCS measurements confirmed association of the WTGal3 with pristine and integrin containing membranes and revealed the existence of two Gal3 populations with distinct diffusivity behaviors that formed on both, pristine and the $\alpha_5\beta_1$ integrin-containing membranes: a dynamic mobile and a slow diffusive one. In the absence of the integrin, the fast moving component had diffusivity values in the range of those observed for the bulk lipid ATTO532-DOPE (6.5 ± 0.15 vs 6.99 ± 0.12, $\mu m^2/s$ respectively), suggesting passive association of the lectin at the pristine membrane. In contrast, diffusivity of the fast component was significantly decreased in $\alpha_5\beta_1$ integrin-containing membranes when compared to the bulk lipid marker (3.54 ± 0.11 vs 5.40 ± 0.40 $\mu m^2/s$, respectively), which suggested that Gal3 binds to the integrin. Notably, incubation of WTGal3 was observed to increase diffusivity of the integrin at the membrane and also altered the diffusion regime from subdiffusion to Brownian diffusion. However, it was evident from time traces that a portion of the integrin is also immobilised on galectin

treatment from photobleaching and FLIM imaging. These observed increase in diffusion of the mobile integrin at the membrane is attributed to the reduction of concentration mobile integrin in the membrane after some of it is sequestered into WTGal3 networks. The reduced protein concentration leads to faster protein diffusion by normal Brownian motion in regions of the membrane that are less crowded after network association.

Moreover, the diffusivity rates of both mobile $\alpha_5\beta_1$ integrin fraction and the fast diffusion sub-population of WTGal3 followed the same trend. That exact matching of integrin and galectin diffusion rates was not observed, and that a substantial portion of integrin remains mobile after galectin treatment can be ascribed to the orientation of the integrin within the membrane: the inner oriented pool (expected to be roughly 50% of integrin) is a priori not exposed to the exogenously added Gal3 and therefore may not be influenced by it, creating an asymmetry in integrin lateral diffusivity. The population of integrin oriented inward will only be influenced by general membrane parameters. This is evident from cross-correlation data in FCS which shows that a sub-population of the integrin and galectin co-diffuse. In addition FCS data show integrin bleaching in the presence of galectin 3 that along with FLIM imaging indicate a significant sub-population of the integrin becomes immobilised on WTGal 3 exposure

In conclusion, we demonstrate that WTGal3 binds in a carbohydrate-dependent manner to $\alpha_5\beta_1$ integrin in MSLB. EIS and FCS studies indicate that this binding occurs in a cooperative process involving the oligomerization of WTGal3 through its N-terminal domain. Very few biophysical models of integrin-galectin interaction have been reported to date. With the emerging importance of this interaction across a diverse range of diseases, microcavity suspended bilayers represent a versatile platform to study such interactions and may provide important biomedically relevant insights at the molecular level extricated from the complexity of the cell.

Author contributions

L.J. and T.E.K. originated the research idea and contributed to experimental design. N.K.S., G.B.B., J.R., M.S.Z., E.D., A.D and D.L contributed to experimental design, performed the experiments and completed the data analyses. L.J. and T.E.K. contributed new reagents or analytic tools. N.K.S., G.B.B., J.R., M.S.Z., E.D., L.J., and T.E.K. wrote the manuscript.

Acknowledgement

TEK, JR, GBB and NKS gratefully acknowledge Science Foundation Ireland under [14/IA/2488], TEK and JR gratefully acknowledge The Irish Research Council for Postgraduate Studentship funding, and LJ gratefully acknowledges Mizutani Foundation for Glycosciences (reference n° 200014), Agence National de la Recherche ANR (ANR-19-CE13-0001-01 and ANR-20-CE15-0009-01), and Fondation pour la Recherche Médicale (EQU202103012926).

References

1. Mouw, J.K., G. Ou, and V.M. Weaver. 2014. Extracellular matrix assembly: a multiscale deconstruction. *Nat. Rev. Mol. Cell Biol. 2014 1512*. 15:771–785.
2. Lee, J.-O., L.A. Bankston, and M.A.A. and Robert C Liddington. 1995. Two conformations of the integrin A-domain (I-domain): a pathway for activation? *Structure*. 3:1333–1340.
3. Margadant, C., I. van den Bout, A.L. van Boxtel, V.L. Thijssen, and A. Sonnenberg. 2012. Epigenetic Regulation of Galectin-3 Expression by β1 Integrins Promotes Cell Adhesion and Migration. *J. Biol. Chem.* 287:44684–44693.
4. Seguin, L., J.S. Desgrosellier, S.M. Weis, and D.A. Cheresh. 2015. Integrins and cancer: regulators of cancer stemness, metastasis, and drug resistance. *Trends Cell Biol.* 25:234–40.
5. Aoudjit, F., and K. Vuori. 2012. Integrin Signaling in Cancer Cell Survival and Chemoresistance. *Chemother. Res. Pract.* 2012:1–16.
6. Bänfer, S., D. Schneider, J. Dewes, M.T. Strauss, S.-A. Freibert, T. Heimerl, U.G. Maier, H.-P. Elsässer, R. Jungmann, and R. Jacob. 2018. Molecular mechanism to recruit galectin-3 into multivesicular bodies for polarized exosomal secretion. *Proc. Natl. Acad. Sci.* 115:E4396–E4405.
7. Seelenmeyer, C., S. Wegehingel, I. Tews, M. Künzler, M. Aebi, and W. Nickel. 2005. Cell surface counter receptors are essential components of the unconventional export machinery of galectin-1. *J. Cell Biol.* 171:373–381.
8. Dumic, J., S. Dabelic, and M. Flögel. 2006. Galectin-3: An open-ended story. *Biochim. Biophys. Acta - Gen. Subj.* 1760:616–635.
9. Liu, F.-T., and G.A. Rabinovich. 2005. Galectins as modulators of tumour progression. *Nat. Rev. Cancer*. 5:29–41.
10. Houzelstein, D., I.R. Gonçalves, A.J. Fadden, S.S. Sidhu, D.N.W. Cooper, K. Drickamer, H. Leffler, and F. Poirier. 2004. Phylogenetic Analysis of the Vertebrate Galectin Family. *Mol. Biol. Evol.* 21:1177–1187.

11. Popa, S.J., S.E. Stewart, and K. Moreau. 2018. Unconventional secretion of annexins and galectins. *Semin. Cell Dev. Biol.* 83:42–50.
12. Hayashi, Y., W. Jia, H. Kidoya, F. Muramatsu, Y. Tsukada, and N. Takakura. 2019. Galectin-3 Inhibits Cancer Metastasis by Negatively Regulating Integrin β3 Expression. *Am. J. Pathol.* 189:900–910.
13. Johannes, L., R. Jacob, and H. Leffler. 2018. Galectins at a glance. *J. Cell Sci.* 131.
14. Ruvolo, P.P. 2016. Galectin 3 as a guardian of the tumor microenvironment. *Biochim. Biophys. Acta - Mol. Cell Res.* 1863:427–437.
15. Barondes, S.H., D.N. Cooper, M.A. Gitt, and H. Leffler. 1994. Galectins. Structure and function of a large family of animal lectins. *J. Biol. Chem.* 269:20807–20810.
16. Zhao, Z., X. Xu, H. Cheng, M.C. Miller, Z. He, H. Gu, Z. Zhang, A. Raz, K.H. Mayo, G. Tai, and Y. Zhou. 2021. Galectin-3 N-terminal tail prolines modulate cell activity and glycan-mediated oligomerization/phase separation. *Proc. Natl. Acad. Sci.* 118:e2021074118.
17. Lin, Y.-H., D.-C. Qiu, W.-H. Chang, Y.-Q. Yeh, U.-S. Jeng, F.-T. Liu, and J. Huang. 2017. The intrinsically disordered N-terminal domain of galectin-3 dynamically mediates multisite self-association of the protein through fuzzy interactions. *J. Biol. Chem.* 292:17845–17856.
18. Chiu, Y.-P., Y.-C. Sun, D.-C. Qiu, Y.-H. Lin, Y.-Q. Chen, J.-C. Kuo, and J. Huang. 2020. Liquid-liquid phase separation and extracellular multivalent interactions in the tale of galectin-3. *Nat. Commun.* 11:1229.
19. Friedrichs, J., A. Manninen, D.J. Muller, and J. Helenius. 2008. Galectin-3 Regulates Integrin α2β1-mediated Adhesion to Collagen-I and -IV. *J. Biol. Chem.* 283:32264–32272.
20. Rao, S.P., Z. Wang, R.I. Zuberi, L. Sikora, N.S. Bahaie, B.L. Zuraw, F.-T. Liu, and P. Sriramarao. 2007. Galectin-3 Functions as an Adhesion Molecule to Support Eosinophil Rolling and Adhesion under Conditions of Flow. *J. Immunol.* 179:7800–7807.
21. Goetz, J.G., B. Joshi, P. Lajoie, S.S. Strugnell, T. Scudamore, L.D. Kojic, and I.R. Nabi. 2008. Concerted regulation of focal adhesion dynamics by galectin-3 and tyrosine-phosphorylated caveolin-1. *J. Cell Biol.* 180:1261–1275.
22. Furtak, V., F. Hatcher, and J. Ochieng. 2001. Galectin-3 Mediates the Endocytosis of β-1 Integrins by Breast Carcinoma Cells. *Biochem. Biophys. Res. Commun.* 289:845–850.
23. King, D.R., D.C. Salako, S.K. Arthur-Bentil, A.E. Rubin, J.B. Italiya, J.S. Tan, D.G. Macris, H.K. Neely, J.M. Palka, J.L. Grodin, K. Davis-Bordovsky, M. Faubion, C.S. North, and E.S. Brown. 2021. Relationship between novel inflammatory biomarker galectin-3 and depression symptom severity in a large community-based sample. *J. Affect. Disord.* 281:384–389.
24. Melin, E.O., J. Dereke, M. Thunander, and M. Hillman. 2018. Depression in type 1 diabetes was associated with high levels of circulating galectin-3. *Endocr. Connect.* 7:819–828.
25. Tao, C.-C., K.-M. Cheng, Y.-L. Ma, W.-L. Hsu, Y.-C. Chen, J.-L. Fuh, W.-J. Lee, C.-C. Chao, and E.H.Y. Lee. 2020. Galectin-3 promotes Aβ oligomerization and Aβ toxicity in a mouse model of Alzheimer's disease. *Cell Death Differ.* 27:192–209.
26. Radosavljevic, G., V. Volarevic, I. Jovanovic, M. Milovanovic, N. Pejnovic, N. Arsenijevic, D.K. Hsu, and M.L. Lukic. 2012. The roles of Galectin-3 in autoimmunity and tumor progression. *Immunol. Res.* 52:100–110.
27. Sonnino, S., L. Mauri, V. Chigorno, and A. Prinetti. 2007. Gangliosides as components of lipid membrane domains. *Glycobiology*. 17:1R-13R.
28. Johannes, L., and A. Billet. 2020. Glycosylation and raft endocytosis in cancer. *Cancer Metastasis Rev.* 39:375–396.
29. Lakshminarayan, R., C. Wunder, U. Becken, M.T. Howes, C. Benzing, S. Arumugam, S. Sales, N. Ariotti, V. Chambon, C. Lamaze, D. Loew, A. Shevchenko, K. Gaus, R.G. Parton, and L. Johannes. 2014. Galectin-3 drives glycosphingolipid-dependent biogenesis of clathrin-independent carriers. *Nat. Cell Biol.* 16:592–603.
30. Johannes, L., C. Wunder, and M. Shafaq-Zadah. 2016. Glycolipids and Lectins in Endocytic Uptake Processes. *J. Mol. Biol.* 428:4792–4818.
31. Renard, H.-F., F. Tyckaert, C. Lo Giudice, T. Hirsch, C.A. Valades-Cruz, C. Lemaigre, M. Shafaq-Zadah, C. Wunder, R. Wattiez, L. Johannes, P. van der Bruggen, D. Alsteens, and P. Morsomme. 2020. Endophilin-A3 and Galectin-8 control the clathrin-independent endocytosis of CD166. *Nat. Commun.* 11:1457.
32. Nabi, I.R., J. Shankar, and J.W. Dennis. 2015. The galectin lattice at a glance. *J. Cell Sci.* 128:2213–2219.
33. Mathew, M.P., and J.G. Donaldson. 2018. Distinct cargo-specific response landscapes underpin the complex and nuanced role of galectin–glycan interactions in clathrin-independent endocytosis. *J. Biol. Chem.* 293:7222–7237.
34. Wagner, M.L., and L.K. Tamm. 2000. Tethered polymer-supported planar lipid bilayers for reconstitution of integral membrane proteins: Silane-polyethyleneglycol-lipid as a cushion and covalent linker. *Biophys. J.* 79:1400–1414.
35. Hussain, N.F., A.P. Siegel, Y. Ge, R. Jordan, and C.A. Naumann. 2013. Bilayer asymmetry influences integrin sequestering in raft-mimicking lipid mixtures. *Biophys. J.* 104:2212–2221.
36. Peetla, C., A. Stine, and V. Labhasetwar. 2009. Biophysical Interactions with Model Lipid Membranes: Applications in Drug Discovery and Drug Delivery. *Mol. Pharm.* 6:1264–1276.
37. Li, B., and E. London. 2020. Preparation and Drug Entrapment Properties of Asymmetric Liposomes Containing Cationic and Anionic Lipids. *Langmuir*. 36:12521–12531.
38. Cheng, H.-T., Megha, and E. London. 2009. Preparation and Properties of Asymmetric Vesicles That Mimic Cell Membranes. *J. Biol. Chem.* 284:6079–6092.
39. Zhang, L., and S. Granick. 2005. Lipid diffusion compared in outer and inner leaflets of planar supported bilayers. *J. Chem. Phys.* 123:211104.
40. Murray, D.H., L.K. Tamm, and V. Kiessling. 2009. Supported double membranes. *J. Struct. Biol.* 168:183–189.
41. McGillivray, D.J., G. Valincius, D.J. Vanderah, W. Febo-Ayala, J.T. Woodward, F. Heinrich, J.J. Kasianowicz, and M. Lösche. 2007. Molecular-scale structural and functional characterization of sparsely tethered bilayer lipid membranes. *Biointerphases*. 2:21–33.
42. Sarangi, N.K., and A. Patnaik. 2012. <scp>L</scp> -Tryptophan-Induced Electron Transport across Supported Lipid Bilayers: an Alkyl-Chain Tilt-Angle, and Bilayer-Symmetry Dependence. *ChemPhysChem*. 13:4258–4270.
43. Gufler, P.C., D. Pum, U.B. Sleytr, and B. Schuster. 2004. Highly robust lipid membranes on crystalline S-layer supports investigated by electrochemical impedance spectroscopy. *Biochim. Biophys. Acta - Biomembr.* 1661:154–165.
44. Hillman, A.R., K.S. Ryder, E. Madrid, A.W. Burley, R.J. Wiltshire, J. Merotra, M. Grau, S.L. Horswell, A. Glidle, R.M. Dalgliesh, A. Hughes, R. Cubitt, and A. Wildes. 2010. Structure and dynamics of phospholipid bilayer films under electrochemical control. *Faraday Discuss.* 145:357–379.

45. Steinem, C., A. Janshoff, W.P. Ulrich, M. Sieber, and H.J. Galla. 1996. Impedance analysis of supported lipid bilayer membranes: A scrutiny of different preparation techniques. *Biochim. Biophys. Acta - Biomembr.* 1279:169–180.
46. McGillivray, D.J., G. Valincius, F. Heinrich, J.W.F. Robertson, D.J. Vanderah, W. Febo-Ayala, I. Ignatjev, M. Lösche, and J.J. Kasianowicz. 2009. Structure of functional Staphylococcus aureus α-hemolysin channels in tethered bilayer lipid membranes. *Biophys. J.* 96:1547–1553.
47. Wiegand, G., N. Arribas-Layton, H. Hillebrandt, E. Sackmann, and P. Wagner. 2002. Electrical properties of supported lipid bilayer membranes. *J. Phys. Chem. B*. 106:4245–4254.
48. Su, Z., J. Jay Leitch, F. Abbasi, R.J. Faragher, A.L. Schwan, and J. Lipkowski. 2018. EIS and PM-IRRAS studies of alamethicin ion channels in a tethered lipid bilayer. *J. Electroanal. Chem.* 812:213–220.
49. Abbasi, F., J.J. Leitch, Z. Su, G. Szymanski, and J. Lipkowski. 2018. Direct visualization of alamethicin ion pores formed in a floating phospholipid membrane supported on a gold electrode surface. *Electrochim. Acta*. 267:195–205.
50. and, J.D., and C. Steinem*. 2003. Pore-Suspending Lipid Bilayers on Porous Alumina Investigated by Electrical Impedance Spectroscopy. .
51. Orth, A., L. Johannes, W. Römer, and C. Steinem. 2012. Creating and modulating microdomains in pore-spanning membranes. *ChemPhysChem*. 13:108–114.
52. Ronen, R., Y. Kaufman, and V. Freger. 2017. Formation of pore-spanning lipid membrane and cross-membrane water and ion transport. *J. Memb. Sci.* 523:247–254.
53. Jose, B., C.T. Mallon, R.J. Forster, C. Blackledge, and T.E. Keyes. 2011. Lipid bilayer assembly at a gold nanocavity array. *Chem. Commun.* 47:12530–12532.
54. Basit, H., V. Gaul, S. Maher, R.J. Forster, and T.E. Keyes. 2015. Aqueous-filled polymer microcavity arrays: versatile & stable lipid bilayer platforms offering high lateral mobility to incorporated membrane proteins. *Analyst*. 140:3012–3018.
55. Berselli, G.B., N.K. Sarangi, S. Ramadurai, P. V. Murphy, and T.E. Keyes. 2019. Microcavity-Supported Lipid Membranes: Versatile Platforms for Building Asymmetric Lipid Bilayers and for Protein Recognition. *ACS Appl. Bio Mater.* 2:3404–3417.
56. Berselli, G.B., N.K. Sarangi, A. V. Gimenez, P. V. Murphy, and T.E. Keyes. 2020. Microcavity array supported lipid bilayer models of ganglioside - influenza hemagglutinin1binding. *Chem. Commun.* 56:11251–11254.
57. Robinson, J., G.B. Berselli, M.G. Ryadnov, and T.E. Keyes. 2020. Annexin v Drives Stabilization of Damaged Asymmetric Phospholipid Bilayers. *Langmuir*. 36:5454–5465.
58. Ramadurai, S., N.K. Sarangi, S. Maher, N. MacConnell, A.M. Bond, D. McDaid, D. Flynn, and T.E. Keyes. 2019. Microcavity-Supported Lipid Bilayers; Evaluation of Drug–Lipid Membrane Interactions by Electrochemical Impedance and Fluorescence Correlation Spectroscopy. *Langmuir*. 35:8095–8109.
59. Ramadurai, S., A. Kohut, N.K. Sarangi, O. Zholobko, V.A. Baulin, A. Voronov, and T.E. Keyes. 2019. Macromolecular inversion-driven polymer insertion into model lipid bilayer membranes. *J. Colloid Interface Sci.* 542:483–494.
60. Sarangi, N.K., A. Prabhakaran, and T.E. Keyes. 2020. Interaction of Miltefosine with Microcavity Supported Lipid Membrane: Biophysical Insights from Electrochemical Impedance Spectroscopy. *Electroanalysis*. 32:2936–2945.
61. Sarangi, N.K., A. Stalcup, and T.E. Keyes. 2020. The Impact of Membrane Composition and Co-Drug Synergistic Effects on Vancomycin Association with Model Membranes from Electrochemical Impedance Spectroscopy. *ChemElectroChem*. 7:4535–4542.
62. Johansson, S., E. Forsberg, and B. Lundgren. 1987. Comparison of fibronectin receptors from rat hepatocytes and fibroblasts. *J. Biol. Chem.* 262:7819–7824.
63. Berselli, G.B., N.K. Sarangi, S. Ramadurai, P.V. Murphy, and T.E. Keyes. 2019. Microcavity-Supported Lipid Membranes: Versatile Platforms for Building Asymmetric Lipid Bilayers and for Protein Recognition. *ACS Appl. Bio Mater.* 2.
64. Maher, S., H. Basit, R.J. Forster, and T.E. Keyes. 2016. Micron dimensioned cavity array supported lipid bilayers for the electrochemical investigation of ionophore activity. *Bioelectrochemistry*. 112:16–23.
65. Lukyanov, P., V. Furtak, and J. Ochieng. 2005. Galectin-3 interacts with membrane lipids and penetrates the lipid bilayer. *Biochem. Biophys. Res. Commun.* 338:1031–1036.
66. Chung, M., R.D. Lowe, Y.-H.M. Chan, P. V. Ganesan, and S.G. Boxer. 2009. DNA-tethered membranes formed by giant vesicle rupture. *J. Struct. Biol.* 168:190–199.
67. Weng, K.C., J.L. Kanter, W.H. Robinson, and C.W. Frank. 2006. Fluid supported lipid bilayers containing monosialoganglioside GM1: A QCM-D and FRAP study. *Colloids Surfaces B Biointerfaces*. 50:76–84.
68. Johnson, M.A., S. Seifert, H.I. Petrache, and A.C. Kimble-Hill. 2014. Phase Coexistence in Single-Lipid Membranes Induced by Buffering Agents. *Langmuir*. 30:9880–9885.
69. Gaul, V., S.G. Lopez, B.R. Lentz, N. Moran, R.J. Forster, and T.E. Keyes. 2015. The lateral diffusion and fibrinogen induced clustering of platelet integrin αIIbβ3 reconstituted into physiologically mimetic GUVs. *Integr. Biol. (United Kingdom)*. 7:402–411.
70. Yang, R.-Y., P.N. Hill, D.K. Hsu, and F.-T. Liu. 1998. Role of the Carboxyl-Terminal Lectin Domain in Self-Association of Galectin-3. *Biochemistry*. 37:4086–4092.
71. Lepur, A., E. Salomonsson, U.J. Nilsson, and H. Leffler. 2012. Ligand Induced Galectin-3 Protein Self-association. *J. Biol. Chem.* 287:21751–21756.
72. Vaz, W.L.C., F. Goodsaid-Zalduondo, and K. Jacobson. 1984. Lateral diffusion of lipids and proteins in bilayer membranes. *FEBS Lett.* 174:199–207.
73. Saxton, M.J. 1987. Lateral diffusion in an archipelago. The effect of mobile obstacles. *Biophys. J.* 52:989–997.
74. Pearce, K.H., M. Hof, B.R. Lentz, and N.L. Thompson. 1993. Comparison of the membrane binding kinetics of bovine prothrombin and its fragment 1. *J. Biol. Chem.* 268:22984–22991.
75. Yang, E.H., J. Rode, M.A. Howlader, M. Eckermann, J.T. Santos, D. Hernandez Armada, R. Zheng, C. Zou, and C.W. Cairo. 2017. Galectin-3 alters the lateral mobility and clustering of β1-integrin receptors. *PLoS One*. 12:e0184378.
76. Scott, H.L., and T.J. Coe. 1983. A theoretical study of lipid-protein interactions in bilayers. *Biophys. J.* 42:219–224.
77. Stewart, S.E., A. Ashkenazi, A. Williamson, D.C. Rubinsztein, and K. Moreau. 2018. Transbilayer phospholipid movement facilitates annexin translocation across membranes. *J. Cell Sci.*
78. Sych, T., Y. Mély, and W. Römer. 2018. Lipid self-assembly and lectin-induced reorganization of the plasma membrane. *Philos. Trans. R. Soc. B Biol. Sci.* 373:20170117.
79. Maier, O., S.A. Marvin, H. Wodrich, E.M. Campbell, and C.M. Wiethoff. 2012. Spatiotemporal Dynamics of Adenovirus Membrane Rupture and Endosomal Escape. *J. Virol.* 86:10821–10828.